Front. Optoelectron. 2018, 11(2): 163–188
https://doi.org/10.1007/s12200-018-0813-1

REVIEW ARTICLE

# Optical signal processing based on silicon photonics waveguide Bragg gratings: review

**Saket KAUSHAL[1], Rui Cheng[2], Minglei Ma[2], Ajay Mistry[2], Maurizio Burla[1,3], Lukas Chrostowski (✉)[2], José Azaña (✉)[1]**

1 Institut National de la Recherche Scientifique – Centre Energie, Matériaux et Télécommunications (INRS-EMT), Varennes, QC J3X 1S2 Canada
2 Department of Electrical and Computer Engineering, University of British Columbia (UBC), Vancouver, British Columbia, V6T 1Z4 Canada
3 Institute of Electromagnetic Fields, ETH Zurich, Gloriastrasse 35, Zurich 8092, Switzerland



**Abstract** This paper reviews the work done by researchers at INRS and UBC in the field of integrated microwave photonics (IMWPs) using silicon based waveguide Bragg gratings (WBGs). The grating design methodology is discussed in detail, including practical device fabrication considerations. On-chip implementations of various fundamental photonic signal processing units, including Fourier transformers, Hilbert transformers, ultrafast pulse shapers etc., are reviewed. Recent progress on WBGs-based IMWP subsystems, such as true time delay elements, phase shifters, real time frequency identification systems, is also discussed.

**Keywords** silicon photonics, ultrafast optical signal processing, integrated microwave photonics (IMWPs)

## 1 Introduction

Microwave-based wireless communication is ubiquitous. Wide spread adoption of wireless communication in radars, airports, malls, hospitals, satellites, last mile connectivity etc., has created an exponential bandwidth demand, into the THz range [1]. To tackle this unprecedented need for higher bandwidth in wireless communications, recently Federal Communications Commission (FCC) permitted the unlicensed operation in 57 – 71 GHz V band. Moreover, in contrast to free-space optical links, sub-terahertz waves are less affected by adverse weather conditions like rain and fog [1]. Such a burgeoning demand has been fueled by the evolution of digital signal processors (DSPs) [2]. However, there is a need for highly flexible analog radio frequency (RF) signal processors to leverage this rapid evolution of DSPs [3]. Current analog signal processors suffer from low bandwidth, are complex, bulky, and/or offer limited functionality [4,5]. A microwave photonic (MWP) signal processor is a photonic counterpart of an analog RF signal processor, wherein all-optical signal processing enables high frequency and ultra-broadband operation (easily into the THZ range), with electromagnetic interference (EMI) immunity [6,7]. Moreover, MWP solutions offer the potential for implementation of reconfigurable signal processing platforms and have inherently low RF losses [8,9]. Integrated microwave photonics (IMWP) based processors, wherein the subsystem is entirely integrated on a chip, can provide the performance specifications that are desired for practical applications, in terms of reduced power consumption, compactness, low cost etc [10]. This has been largely possible due to the adoption of silicon photonics technology to implement key microwave functionalities on-chip [11,12]. Silicon's high refractive index contrast with air/native oxide allows compact bends in rings, as well as high refractive index modulation in gratings and cavities, which leads to compact form factors, in the $\mu m^2$ range, compared to silica or InP platforms, with typical form factors above $mm^2$ [13]. Silicon also benefits from fairly well established and highly matured complementary metal-oxide semiconductor (CMOS) based foundry processes for fabrication of on-chip photonic integrated circuits (PICs) and devices [14]. Leading CMOS foundries, such as IMEC, IME and others, now provide dedicated silicon photonic process design kits (PDKs) [14].

A key element in any IMWP signal processor is a linear photonic filtering device capable of providing a user-defined response, according to the specifications of the target application (bandpass/bandstop filtering; customized

Received March 19, 2018; accepted May 15, 2018

E-mails: lukasc@ece.ubc.ca, azana@emt.inrs.ca

Invited Paper, Special Issue—Photonics Research in Canada

phase/delay devices etc.); In this regard, waveguide Bragg gratings (WBGs) are an extremely attractive solution [15] because of 1) the versatility by which one can design any desired spectral/temporal linear response by properly synthesizing the main grating parameters [16–22], and 2) their potential for broadband operation, easily reaching the THz range, in a very compact format (typically with sub-mm device length) [17,18]. With progress in 193 nm lithography, it is now possible to fabricate wafer-scale low loss gratings with minimal fabrication imperfections on silicon [23].

This article summarizes the work done in the past decade or so by researchers at the Ultrafast Optical Processing group of Prof. José Azaña at INRS in collaboration with Prof. Lukas Chrostowski's group at UBC, in the field of IMWPs using silicon-based WBGs. This review article is divided into 5 sections. Section 2 describes the design methodology and fabrication process flow of WBGs. Given a target amplitude and phase response, how to extract grating design parameters viz. period, corrugation strength, apodization profile etc. will be discussed in detail. Impact of fabrication imperfections on the obtained spectral responses will be reviewed as well. Sections 3 and 4 discuss a host of applications in ultrafast optical processing and MWPs already demonstrated on ultra compact silicon-on-insulator (SOI) platforms. Finally we summarize the article.

## 2 Design of Bragg gratings on silicon-on-insulator (SOI) platform

### 2.1 Introduction

Bragg gratings are structures with a periodic perturbation of the effective refractive index along the length. These components were initially fabricated on optical fibers, by exposing photosensitive fibers to ultraviolet (UV) light beam [15]. This way, an optical interference pattern can be imposed on the fiber, producing a periodic effective refractive index change along the fiber. Such in-fiber Bragg gratings have been used as basic building blocks for numerous applications in fiber communications and fiber sensing networks [24]. Recently, significant interest has also gone into realizing Bragg grating devices in integrated waveguides, particularly, on the silicon-on-insulator (SOI) platform [14,20]. Due to compatibility with CMOS fabrication, SOI is considered as a promising platform for ultra-dense on-chip integration of photonic and electronic circuitry. Thus, building Bragg grating devices in SOI as versatile filters is of great interest for many on-chip applications such as wavelength-division multiplexing (WDM) and photonic signal processing. Figure 1(a) shows the cross-sectional view of a SOI wafer. The typical 200 mm wafer consists of a 725 μm silicon substrate, 2 μm of oxide (buried oxide, or BOX), and 220 nm of crystalline silicon. There are two different types of waveguide geometries that can be used to implement WBGs in silicon. The most common geometry is the strip waveguide, as shown in the left of Fig. 1(b). The typical dimension for single mode strip waveguide is 220 nm thick × 500 nm wide. In addition, WBGs can also be fabricated on rib waveguide, as shown in the right of Fig. 1(b). Such rib waveguides are usually used for electro-optic devices such as modulators since they allow for electrical connections to be made to the waveguide [25]. The most common form of WBGs are formed by side-wall modulation along the waveguide, as shown in Figs. 2(a) and 2(b), where $\Delta W$ is the amplitude of the side-wall modulation, or called the corrugation width. Such a side-wall modulation can lead to an equivalent periodic perturbation of the effective refractive index along the integrated waveguide. The effective index of the fundamental TE mode for a typical 220 nm thick × 500 nm wide single-mode silicon waveguide is ~2.44 around 1.55 μm [14]. Thus, to obtain a Bragg resonance at ~1.55 μm, the period of a Bragg grating should be designed to be near 317 nm.

Bragg gratings are characterized by their easy fabrication, low insertion loss, and high extinction ratio. But the most distinguishing feature is the flexibility in their amplitude and phase spectral responses. Almost any

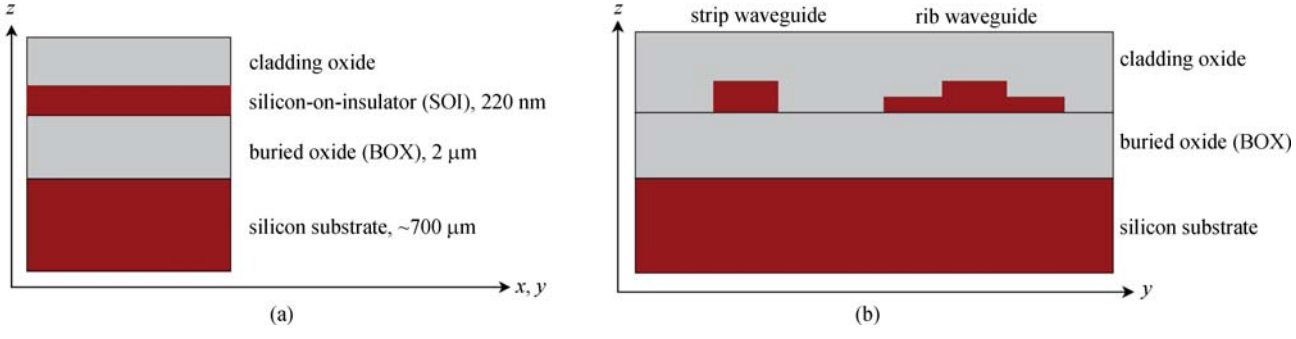


**Fig. 1** (a) Cross-sectional view of silicon-on-insulator (SOI) wafer. (b) Common waveguides in silicon photonics. (Left) Strip waveguide, also known as channel waveguides, photonic wires, or ridge waveguides. (Right) Rib waveguide, also known as ridge waveguide or strip-loaded ridge waveguide; Reproduced from Ref. [14]

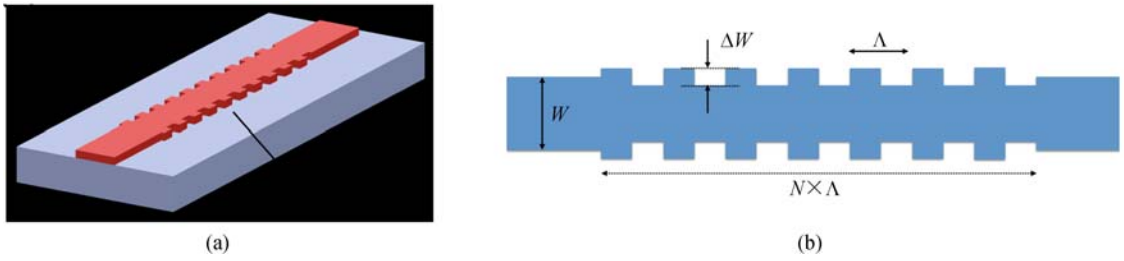


**Fig. 2** Schematic illustration of a typical side-wall waveguide Bragg grating (WBG). $W$: waveguide width; $\Delta W$: corrugation width; $\Lambda$: grating period; $N$: number of the periods

physically realizable spectral response can be tailored on Bragg gratings by modulating the coupling coefficient along the grating. This spectral versatility makes them particularly suitable for use in MWPs signal processing applications, where a well-defined complex spectral response is usually required. Figure 3 illustrates a general design flow of an integrated Bragg grating for a desired spectral response. The first step of the design is to calculate the required coupling coefficient profile from the target spectral response, through various tools such as the layer peeling algorithm [26]. Then, one can select a grating apodization method, such as corrugation width modulation, to translate the coupling coefficient profile to the grating structure. Once the structure of the grating has been determined, the layout is created which is then sent for fabrication. Finally, the spectral response of the fabricated grating is measured and the experimental results is compared with the target spectral response. This cycle may be repeated until a satisfied spectral response is obtained. In the following sections, we will review more details about the design process of WBGs.

## 2.2 Calculation of the apodization profile from the target spectral response

The first step in designing a WBGs for a target spectral response is to calculate the required apodization profile, that is the coupling coefficient profile along the grating. The most straightforward approach for this purpose is to obtain the required apodization profile directly from the temporal impulse response of the target spectral response [26]. This method exploits a first-order Born approximation and is simple to be implemented. However, as the approximation only considers the first reflection from the medium, the method is only accurate when the weak coupling condition is satisfied in the grating.

To overcome this limitation, more powerful layer-peeling (sometimes called “differential inverse scattering”) based approaches have been used for the synthesis of WBGs [26]. Such an approach is based on finding the grating structure from the reflection spectrum simply by propagating the electromagnetic fields along the grating structure, while simultaneously evaluating the grating

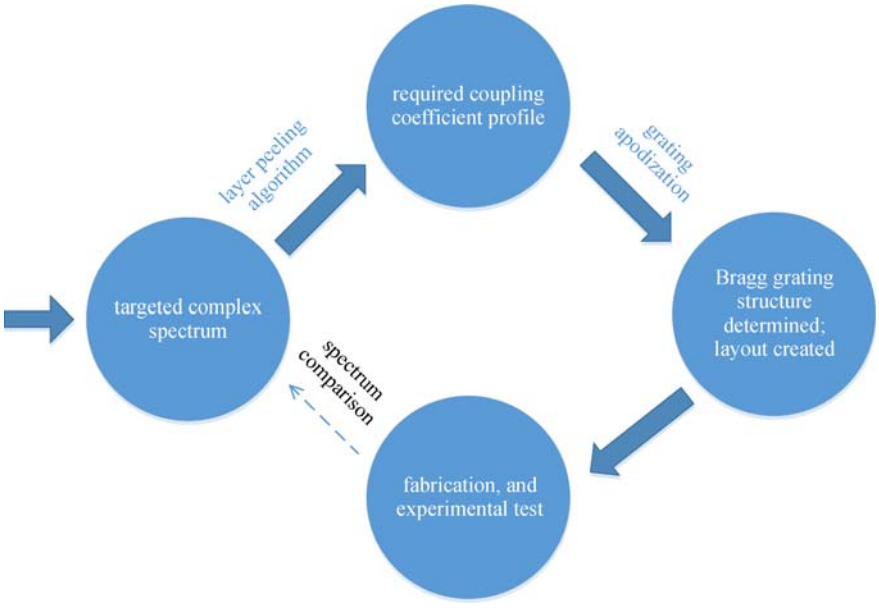


**Fig. 3** A typical design flow of an integrated Bragg grating for a target spectral response

strength using a simple causality argument [26]. The principle and implementation details can be found in Ref. [26]. WBGs based Hilbert transformers [27] and bandpass rectangular-shaped dispersion-less filters [28], have been designed and demonstrated using this method. For example, a typical amplitude and phase response of a photonic Hilbert transformer is shown in Fig. 4(a). Using layer peeling algorithm, Fig. 4(b) depicts the corresponding apodization profile required to obtain the target response. One can see in Fig. 4(b) that the required apodization profile is complex with a large dynamic range in the index modulation. This imposes a high demand on the coupling coefficient modulation, which should have a high accuracy, reliability, and a large dynamic range, while maintaining a constant effective refractive index and thus a constant Bragg wavelength, as we will discuss later in next sections.

### 2.3 Coupling coefficient modulation for Bragg gratings

In this section, we will review different schemes for the modulation of coupling coefficient, $\kappa$, for WBGs. The most straightforward approach for $\kappa$ modulation is to simply change the corrugation width (denoted as $\Delta W$ in Fig. 2(b)) along the grating. Such corrugation-width modulated gratings have advantages of simplicity and ease of fabrication. However, due to the strong overlap between the guided mode and the perturbation, even a small variation in the side-wall amplitude can modify the coupling coefficient significantly. Therefore, the precision and resolution of this modulation is limited by the fabrication constraints such as lithography resolution [30,31].

Different apodization methods have been proposed to overcome the limitation of the conventional $\Delta W$ modulation method. Tan et al. in Ref. [32] proposed novel cladding-modulated WBGs. Instead of conventional side-wall WBGs, such cladding-modulated WBGs are formed by placing periodic silicon cylinders in the cladding at a fixed distance (denoted as $d$) from a single-mode silicon waveguide, as illustrated in Fig. 5. The coupling strength of such grating structures can be controlled by changing the diameter $W$ and the distance of the periodically placed silicon cylinders. Due to a weaker overlap between the light mode and the index perturbation structures compared with conventional side-wall WBGs, cladding-modulated gratings can easily achieve a weak $\kappa$ and thus allow narrow-band spectra to be obtained. Also, as the strength of mode coupling can be varied by adjusting the distance of the cylinders to the waveguide, the $\kappa$ modulation has an improved resolution. Coupling strengths differing by 1 order of magnitude were demonstrated in Ref. [32]. A reflection bandwidth as small as 0.6 nm and a high extinction ratio of 21.4 dB in the transmission have been demonstrated using this cladding modulated method [33]. Nevertheless, this method has not been used for the modulation of complicated apodization profiles, which are usually required for a well-defined complex spectral responses for MWP applications. Fabrication uniformity and repeatability of such small silicon cylinders remains a challenging task.

In Ref. [31], an apodization scheme based on varying the duty-cycle was pro- posed, as schematically illustrated in Fig. 6(a), where the duty-cycle $DC$ is defined as the ratio of the grating ridge width $d$ to the grating period $\Lambda$, i.e., $DC = d/\Lambda$. In this modulation scheme, $\kappa$ will be modulated by the duty-cycle by the following relationship

$$\kappa \propto \sin(\pi \times DC). \tag{1}$$

In this method, the lower limit of the practically achievable duty cycle is determined by the smallest realizable grating ridge, whereas the upper limit is given by the smallest width of grating grooves that can be fabricated. However, duty cycle modulation based approach can modify the local effective refractive index, which in turn can introduce chirp in the grating that can broaden or distort the spectral response. In principle, such unwanted index changes can be compensated by modifying the period according to the local duty cycle, but this can significantly increase the design complexity.

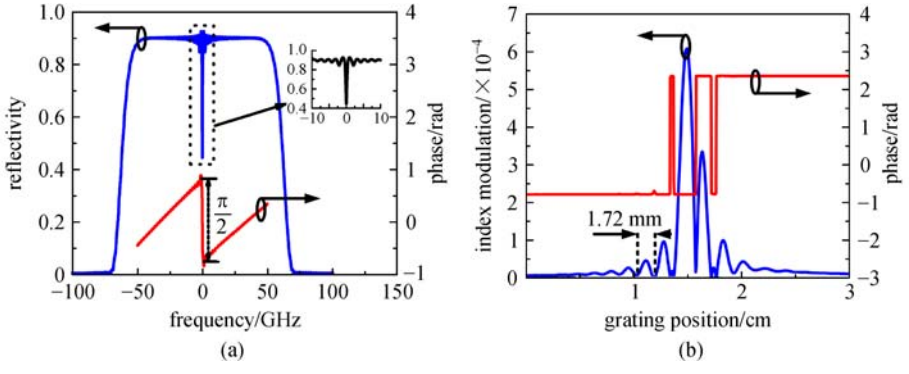


**Fig. 4** (a) Typical amplitude and phase response of a photonic Hilbert transformer. (b) Corresponding apodization profile of a fiber based Bragg grating, obtained using layer peeling algorithm. Reproduced from Ref. [29]

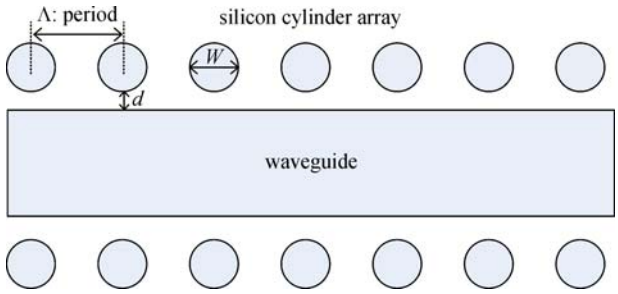


**Fig. 5** Schematic of cladding-modulated waveguide Bragg gratings (WBGs). Λ: period of the silicon cylinders; *W*: diameter of the silicon cylinder; *d*: distance of the silicon cylinders from the edge of the waveguide

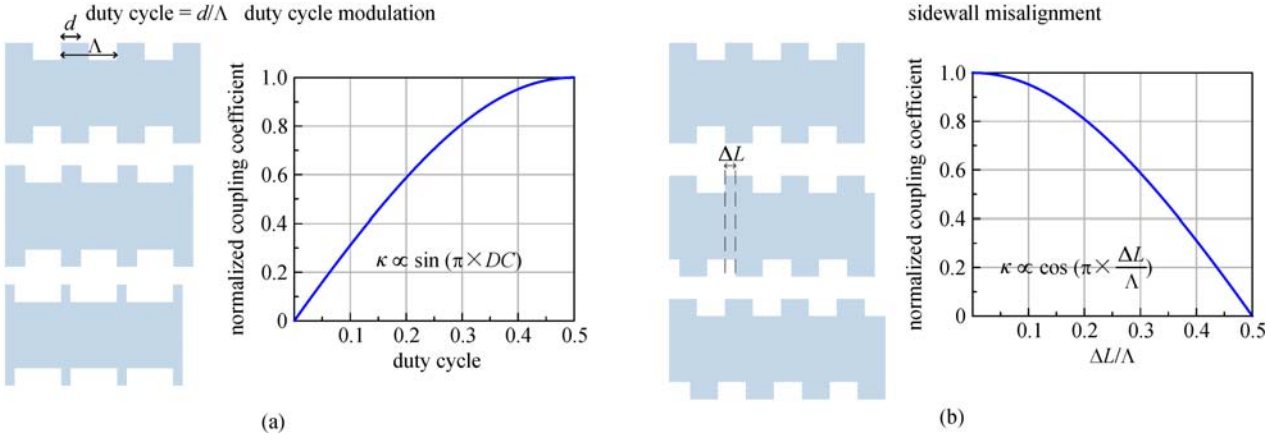


**Fig. 6** (a) (Left) Schematic of grating duty-cycle modulation and (right) the relationship curve between duty cycle and $\kappa$. (b) (Left) Schematic of side-wall miss-alignment modulation and (right) the relationship curve between the miss-alignment and $\kappa$

A novel apodization method where $\kappa$ is varied by intentionally misaligning the corrugations on the two sidewalls was proposed in Refs. [30,34]. The schematic of this apodization approach is illustrated in Fig. 6(b), where $\Delta L$ is the offset between the two side-walls. In this method, $\kappa$ is related to the misalignment $\Delta L$ by the following relationship

$$\kappa \propto \cos\left(\frac{\pi\Delta L}{\lambda}\right). \tag{2}$$

This method can lead to a significant improvement in the resolution, by noting that the minimum effective-index modulation of a conventional Bragg grating can be still reduced by a factor of $\cos(\pi\Delta L/\lambda)$ [34]. High-performance Hilbert transformers recently have been demonstrated in Ref. [16] based on such laterally apodized WBGs, where a processing bandwidth as large as ~750 GHz and a time-bandwidth product above 20 were achieved. However, variations in $\Delta L$ can modify the effective refractive index, which can lead to chirp along the grating and thus broaden and distort the spectral response.

Simard et al. in Ref. [28] proposed a promising phase modulation-based apodization method, where through this approach a narrowband dispersion-less square-shaped filter and bandpass dispersion compensator filter were successfully demonstrated. This method was also exploited to design multi- channel photonic Hilbert transformers [35]. It should be noted that the phase modulation based apodization technique described here is only for controlling the grating strength $\kappa$, while for some phase-shifted gratings, the added phase shift is used to introduce special spectral features, such as opening a narrow-band transmission window [36].The basic idea of the phase modulation-based apodization method is to add a sinusoidally varying phase

$$\phi(z) = A(z)\sin\left(\frac{2\pi z}{\Lambda_M}\right), \tag{3}$$

with a $z$-dependent amplitude $A(z)$ and a period of $\Lambda_M$, into the effective index change along the grating to control the coupling coefficient [30]. The normalized coupling coefficient, $\kappa_N(z)$, will finally be related to the phase amplitude $A(z)$

$$A(z) = J_0^{-1}\left(\kappa_N(z)\right), \tag{4}$$

where $J_0$ is the 0th-order Bessel function.

Thus the apodization of a specific $\kappa(z)$ profile on a WBG

is finally equivalent to applying a phase modulation profile, $\phi(z)$, on the grating, which can be calculated from Eqs. (3) and (4). Then, the task is to map the phase profile onto the grating structure. This can be achieved by modulating the distances between adjacent corrugations, defined as $d(i)$ for the distance between the $i$th and $(i+1)$th period corrugations. Figure 7(a) is a schematic flow showing the process of mapping the apodization profile into a grating structure using the phase modulation method. Figure 7(b) illustrates a typical phase-modulated grating structure. The $d(i)$ distribution along the grating periods can be obtained through

$$d(i) = \frac{\Lambda_G}{2}\left(1 - \frac{\Delta\phi(i)}{\pi}\right), \tag{5}$$

where $\Lambda_G$ is the grating period, and $\Delta\phi(i)$ is the phase difference between $i$th and $(i+1)$th periods.

Figures 7(c)–7(e) illustrate the apodization of a Gaussian profile on a WBG through the phase modulation method, where the grating period $\Lambda_G$ is designed to be 316 nm, corresponding to a Bragg resonance around 1550 nm. The normalized target apodization profile $\kappa(z)$ is plotted (blue) in Fig. 7(c), and the phase amplitude $A(z)$ calculated via Eq. (4) is also shown (red). It can be sen that the phase modulation amplitude decreases with an increase of $\kappa$, and there is no phase modulation [$A(z)$= 0] at the grating region with the highest grating strength. The phase profile, obtained via Eq. (3) is plotted in Fig. 7(d), where the phase period $\Lambda_M$ has been set to 3 μm. To determine the grating structure, the phase profile is finally converted to $d(i)$ distribution along the WBG, as shown in Fig. 7(e). It can be seen that $d(i)$ exhibits an oscillating behavior around $\Lambda_G/2$ (158 nm).

Previous studies have suggested that this phase modulation-based apodization method could be highly promising for use in MWPs applications [28,35]. This is not only because of its high precision, resolution, and dynamic range, but more importantly, the phase modulation has much less impact on the refractive effective index, as we shall see later. Therefore, it allows the achievement of well-controlled amplitude and phase response on WBGs which is essential for MWPs applications. The disadvantage of this scheme is that the spectra of WBGs apodized

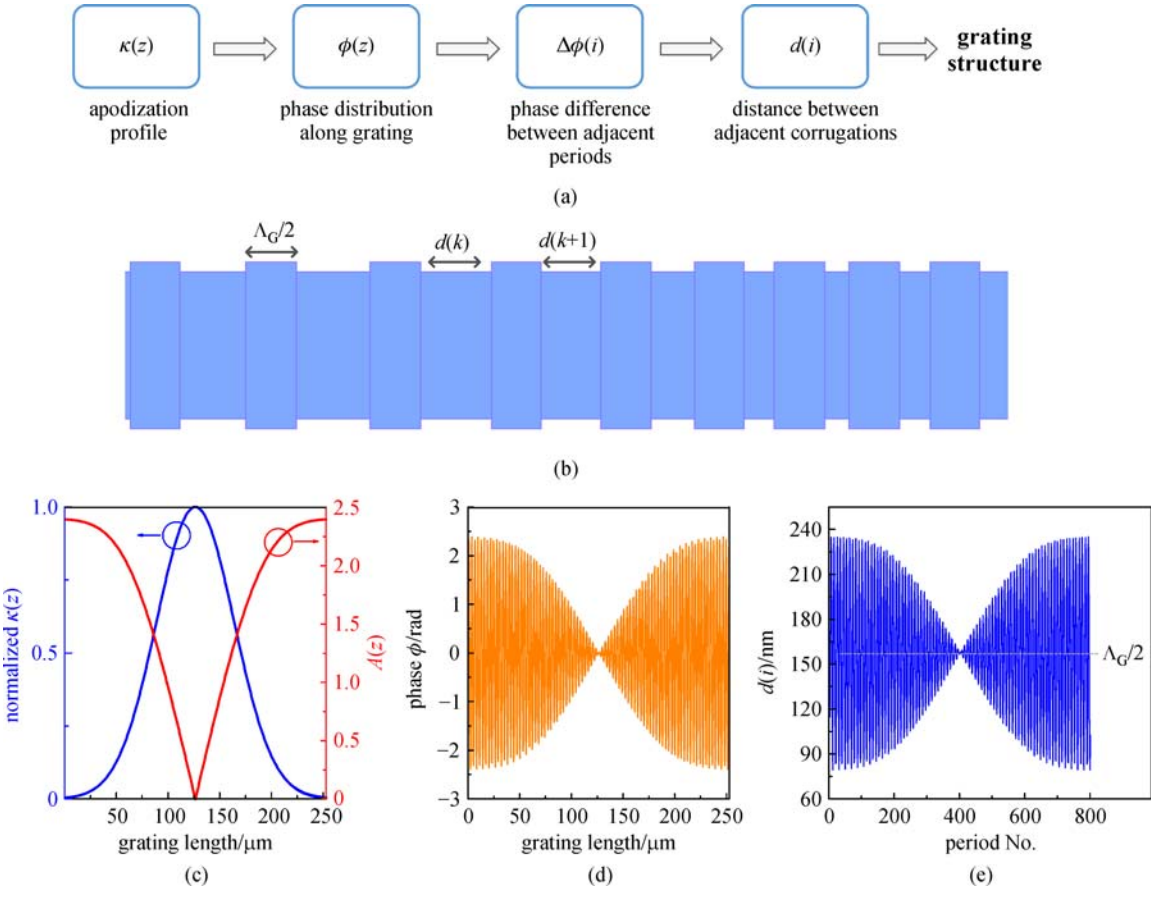


**Fig. 7** (a) Schematic flow showing the process of mapping the apodization profile into grating structure, taken from Ref. [35]. (b) Schematic diagram illustrating a typical phase-modulated grating structure. (c) (Blue) Target Gaussian apodization profile and (red) phase modulation amplitude along the grating $A(z)$. (d) Phase modulation profile along the grating. (e) $d(i)$ distribution along the grating position, where the horizontal line represents the level of $\Lambda_G/2$ (158 nm)

by this method have a relatively high noise floor, due to the accompanying echoes located on both sides of the main spectrum [28,30]. This issue can be mitigated by employing a smaller phase period $\Lambda_M$, at the expense of smaller feature size along the WBG, thus imposing stringent fabrication requirement.

Simulations have been performed to compare the performance of different apodization methods for WBGs. A photonic Hilbert transformer is designed. The amplitude and phase response of the designed Hilbert transformer is shown in Fig. 8(a), which has a bandwidth of 5 nm. The required coupling coefficient profile $\kappa(z)$ is plotted in Fig. 8 (b), obtained using the layer peeling method. We use three different approaches namely phase modulation, side-wall misalignment based modulation, and duty cycle modulation, to apodize the WBGs for a given $\kappa(z)$. Then, the spectral responses are calculated using the standard transfer matrix method (TMM) [14].The TMM method employed is similar to the method used in characterizing optical thin films [37]. Here, a grating apodized by different methods is first discretized along the grating length. Each element is considered as a single layer, with its effective refractive index determined by its average waveguide width. As this TMM approach is directly performed based on the apodized grating structure, the structure modification-induced grating chirp will be taken into account. The effective refractive index versus waveguide width $n_{\text{eff}}(w)$ can be obtained by the eigenmode analysis. It should be noted that $n_{\text{eff}}(w)$ need to be scaled with a factor of about 0.4 when using it into the TMM calculation. This is because of the difference of the waveguide grating with a real optical multi-layer structure, as elaborated further in the treatment of $\delta n_{\text{eff}}$ eigenmode approach in Section 2.5. A full description of the grating spectral characterization method used here will be reported in our future work.

Figures 8(c), 8(d) and 8(e) show the calculated complex spectral responses of the grating apodized by three different methods. It can be seen that the phase modulated grating [Fig. 8(c)] has the best spectral performance and the highest agreement with the target response. For the other two apodization methods shown in Figs. 8(d) and 8 (e), due to the unwanted refractive index changes accompanied by the coupling coefficient modulation, both the amplitude and phase spectral responses are distorted compared to the target response. The distortion in response due to duty cycle modulation is more severe than that of the side-wall misalignment modulation, suggesting that such a coupling coefficient modulation method can introduce a significant refractive index

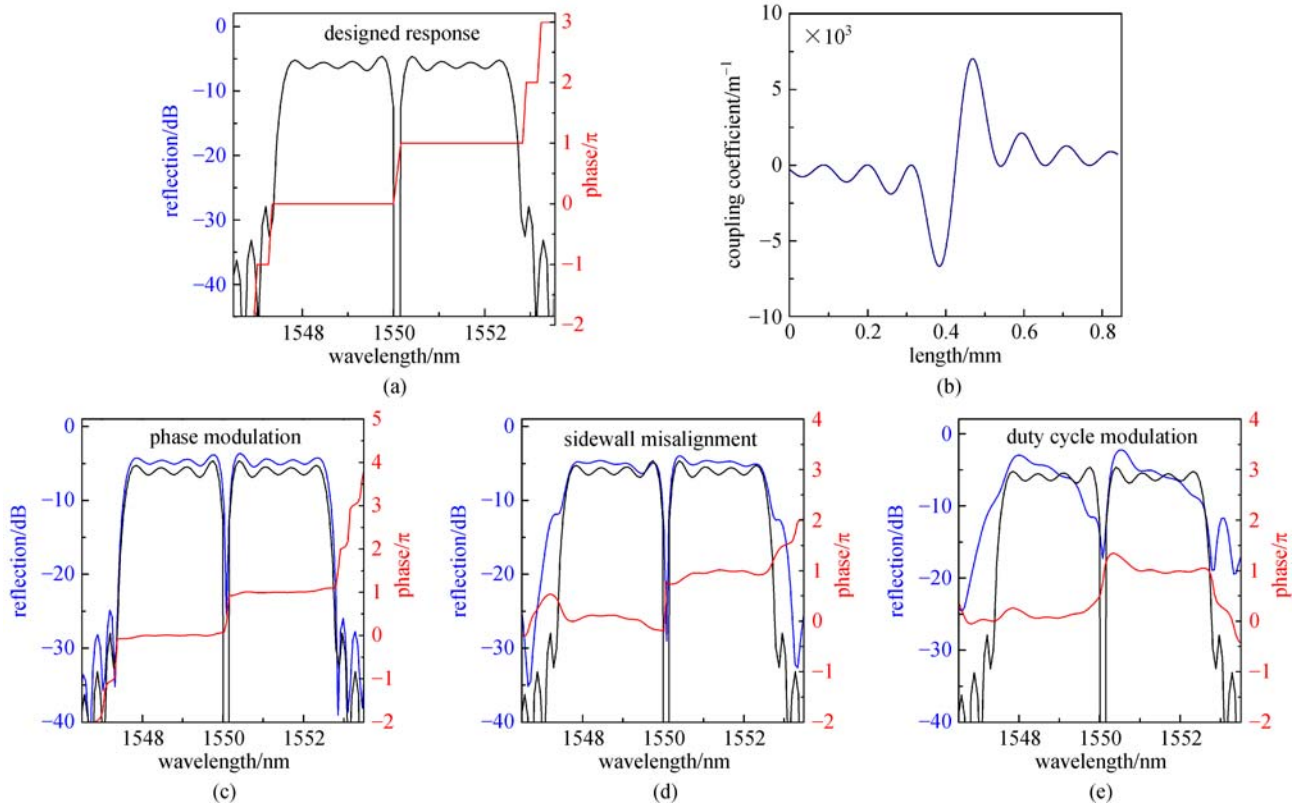


**Fig. 8** (a) Complex spectral response of the designed Hilbert transformer. (b) Required coupling coefficient profile. (c), (d) and (e) are the calculated spectral responses of the gating apodized by the phase modulation method, the side-wall misalignment modulation, and duty cycle modulation, respectively; the spectral calculation is based on the standard transfer matrix method upon the apodized grating structures; the black curves in these figures are the amplitude response of designed Hilbert transformer, shown for comparison

variation that makes it unsuitable for achieving well-controlled complex spectral responses. These results highlight the potential of the phase modulation apodization for MWP applications to achieve advanced and well-controlled complex spectral responses.

### 2.4 Impact of different corrugation widths on the grating spectral responses

The overall amplitude of the apodization profile imposed on an WBG is determined by the corrugation width $\Delta W$ of the WBG. It was suggested in Ref. [26] that different $\Delta W$ will only affect the reflectivity of a grating, as long as weak-coupling condition is satisfied. When $\Delta W$ is larger than the upper-bound of the weak-coupling condition, the spectral response begins to deviate from the designed response. Simulations are performed to investigate the impact of different corrugation width $\Delta W$ on the spectral response, where, again, a photonic Hilbert transformer with a bandwidth of 5 nm is taken as a reference. The phase modulation based apodization is employed in the simulations, and the transfer matrix method is used to calculate the spectral performance. Figure 9 shows the calculated spectral response for different corrugation width $\Delta W$. One can find that the amplitude and phase spectral responses remain relatively unchanged except the reflectivity and agree well with the designed response when $\Delta W$ is smaller than 8 nm. However, when $\Delta W$ is larger than 8 nm, the amplitude response begins to be broadened and the phase jump is increased to be larger than $\pi$, suggesting that the weak-coupling condition is no longer satisfied.

Therefore, we can conclude that the corrugation with $\Delta W$ should be chosen to be as large as possible to obtain a high reflectivity, while still meeting the weak-coupling condition that is essential to retain the target spectral response. Note that the upper bound of $\Delta W$ or the apodization profile amplitude that meet the weak-coupling condition can be different for different target spectral responses. The upper bound of $\Delta W$ may be determined by calculating spectral responses for different $\Delta W$ using TMM method, taking into account the dependence of effective refractive index on the waveguide width. In the next section, we will briefly review how to determine the relation between $\Delta W$ and $\kappa$.

### 2.5 Calculation of the coupling coefficient from a grating structure

In this section, we will review how to calculate the coupling coefficient from a specific grating structure. There are several methods used to extract coupling coefficient for optical structures with mode coupling, namely perturbation analysis based on coupling mode theory (CMT) [38], $\Delta n_{\text{eff}}$ eigenmode approach [14], and band structure calculation in 3D finite difference time-domain (FDTD) [34]. However, not all of these methods

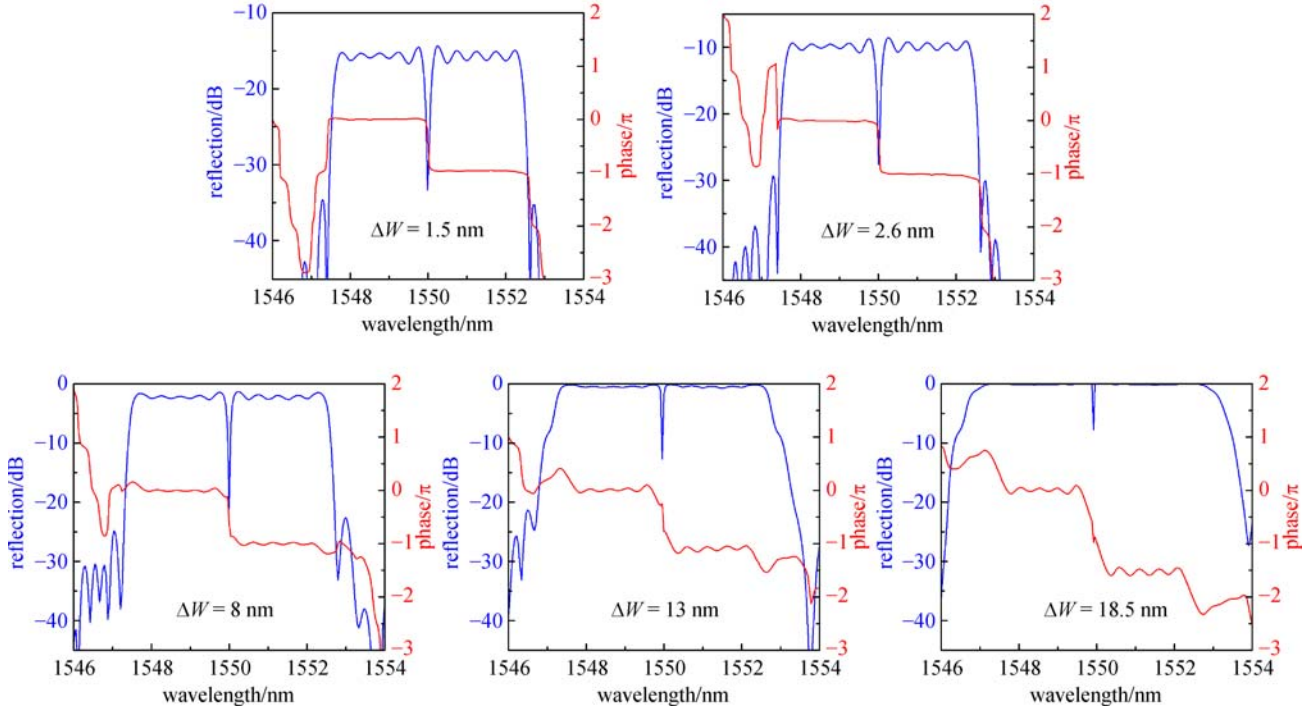


**Fig. 9** Spectral responses of photonic Hilbert transformers based on waveguide Bragg gratings (WBGs) with different corrugation widths, calculated by the transfer matrix method (TMM) method

are accurate when applying for silicon WBGs. In the next, we will review these different methods, and compare their accuracy by comparing the results with the experimental values.

Perturbation analysis method based on coupled-mode theory assumes that the mode coupling is weak, and the coupling occurs between the two modes traveling at the opposite directions. Grating is treated as a medium perturbed by a period refractive index change [39]. The expression of the coupling coefficient obtained in perturbation analysis, as given in Ref. [38], for TE mode is

$$\kappa = \frac{k_0^2}{2\beta N^2}\int_{\text{corrugation}} \Delta[n^2(x,z)]\varepsilon^2(x)\mathrm{d}x, \tag{6}$$

where $k_0 = 2\pi/\lambda_0$ is the free space number, $\beta$ is the TE-mode propagation constant, $\varepsilon$ is the $y$ component of the unperturbed E-field, $n(x, z)$ is the perturbation in refractive index of the corrugation, and $N^2$ is a normalization constant given by

$$N^2 = \int_{-\infty}^{+\infty} \varepsilon^2(x)\mathrm{d}x.$$

By calculating the distribution of $n(x,z)$ for a given grating cell structure, which can be accomplished using eigen-mode analysis, the coupling coefficient of the structure can be obtained. In Ref. [40], this method was used to analyze the coupling coefficient for the grating with a variety of corrugation shapes. However, due to its assumption of the weak coupling, the obtained results will be not accurate when the coupling is strong, i.e., when $\Delta W$ is large.

The second method for $\kappa$ calculation is what we call $\Delta n_{\text{eff}}$ eigenmode approach, and the concept is borrowed from optical thin film characterizations. In this method, grating is considered as a multi-layer thin film, while different width dependent effective refractive indices are treated as different refractive indices of different layers. The underlying concept behind this method is to perform eigenmode analysis to obtain effective refractive indices of the wide and narrow waveguide in the grating, $n_{\text{eff1}}$ and $n_{\text{eff2}}$. Then the differential effective refractive index $\Delta n_{\text{eff}} = n_{\text{eff1}} - n_{\text{eff2}}$ is used to calculate $\kappa$, through either Fresnel equations or the TMM method, as described in Ref. [14]. However, when using this method for side-wall WBGs, because the effective refractive index variations are not totally equivalent to the refractive index variations, the calculated $\kappa$ is not accurate and will be larger than the experimentally obtained $\kappa$ values, as we will see later.

The coupling coefficient of WBGs can also be calculated using 3-D FDTD simulations. However, the FDTD simulation of the whole structure is computationally intensive. If the grating is very weak and long, it can be impractical to run the simulation to get accurate frequency-domain results. Wang et al. in Ref. [34] proposed a way to obtain the coupling coefficient by calculating the band gap of Bragg grating band structures using FDTD. Because this calculation is implemented based on only a unit cell of the grating using Bloch boundary conditions, it is much more efficient than full FDTD simulations. Photonic band structures are similar to electronic band structures in solid- state physics, which describes the range of energies that an electron within the solid may have (called energy bands, allowed bands, or simply bands) and ranges of energy that it may not have (called band gaps or forbidden bands) [41]. Similarly, for the photonic band structures, it indicates frequency range of the photonic material in which the light can transmit or be reflected. The photonic band structure can be calculated by plotting $\omega$-$k$ dispersion diagram for all the Bloch modes.

The left of Fig. 10(a) shows a typical band structure of a uniform optical guiding medium. It is seen that the two Bloch modes are crossing with each other without any gaps, which means that light at all the frequencies can transmit through this uniform medium. The right plot of Fig. 10(a) is a typical band structure for 1-D photonic crystals, where a gap between the two mode lines can be seen. This gap corresponds to the frequency range in which the light is reflected and can not transmit through the medium. WBGs can be considered as a 1-D photonic crystal, and the band gap in such cases can be interpreted as the reflection band, as illustrated in Fig. 10(b).

The location and width of the gap will indicate the center wavelength and bandwidth $\Delta\lambda$ of the Bragg grating respectively. Once $\Delta\lambda$ has been obtained from the band gap, $\kappa$ can be calculated through the following equation [34]

$$\kappa = \pi n_{\text{g}} \Delta\lambda / {\lambda_0}^2, \tag{7}$$

where $n_{\text{g}}$ is the group index of the waveguide. Some commercial optical analysis software, such as Lumerical Inc., can provide a powerful tool for the band structure analysis [42]. Figure 10(c) shows the band structure analysis for a grating unit cell taken from Lumerical FDTD Solutions. By sweeping the Bloch vector $k$ while Fourier transforming the time-domain signals collected by the monitors [yellow X marks in Fig. 10(c)] in the FDTD simulation region, the band structure diagram can be constructed, as plotted in Fig. 10(d). A gap at the band edge can be seen in the diagram. Figure 10(e) plots the Fourier transformed results of the time domain signals at the band edge for gratings with different corrugation width $\Delta W$. The wavelength range between the two peaks corresponds to the band gap. One can find that the width of the gap increases with the $\Delta W$, which means a larger $\Delta\lambda$ and thus a higher $\kappa$ for a grating with a larger $\Delta W$. The band structure method for $\kappa$ determination is accurate, can be used for various grating structures, and is suitable for both strongly and weakly coupled WBGs. Also, it is very efficient, as the analysis can be implemented based on analyzing a single grating cell unit. More theories regarding photonic band structures and the relevant calculation methods can be found in Refs. [43,44].

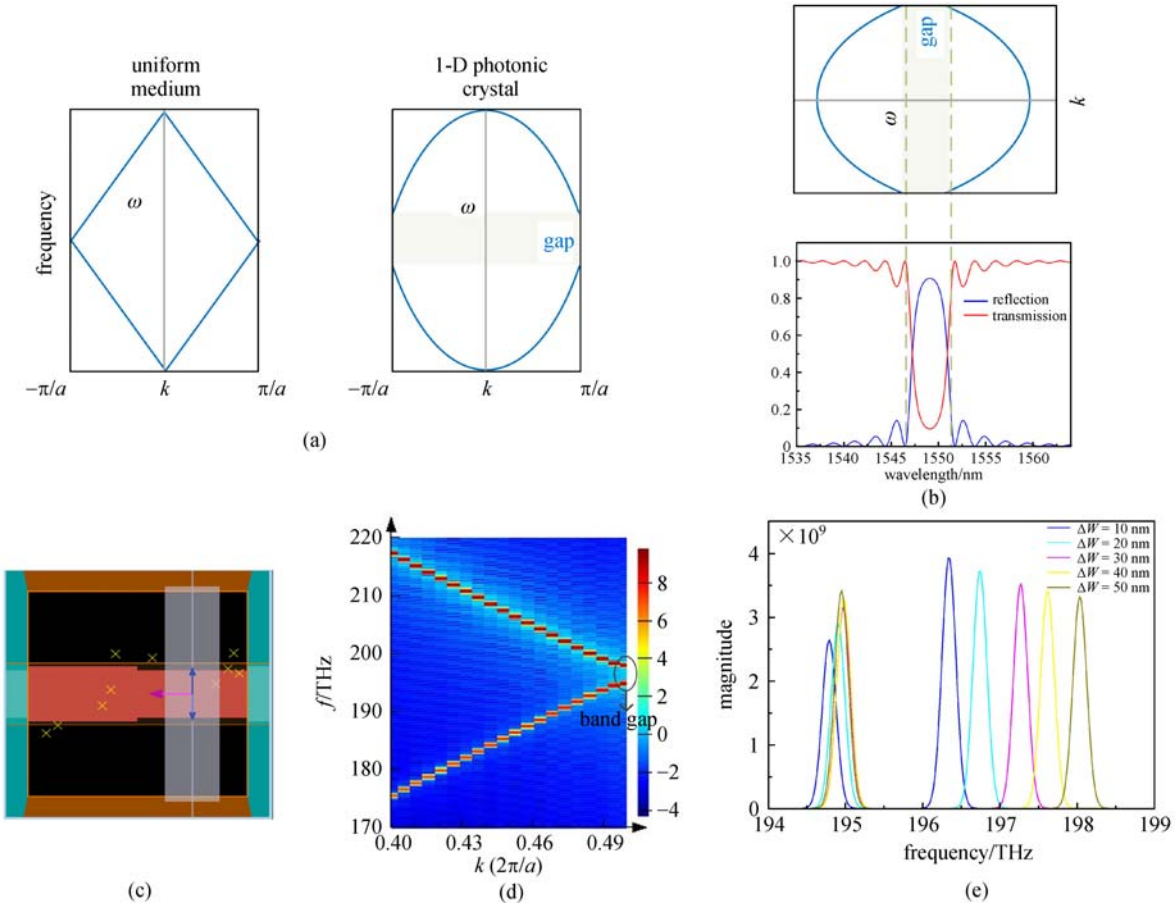


**Fig. 10** (a) Compare of the band structures for uniform medium and 1-D photonic crystal. (b) Schematic illustration of how the band structure is related to the reflection band of a Bragg grating. (c) FDTD band structure analysis in Lumeical FDTD Solutions. (d) Band structure diagram for of a waveguide Bragg grating (WBG) with $\Delta W$ of 50 nm. (e) Fourier transform (magnitude) of the time domain signals at the band edge from the FDTD simulation for WBGs with different $\Delta W$; the frequency range between the two peaks corresponds to the band gap width

To compare the accuracy of the different $\kappa$ calculation approaches described above, we calculate $\kappa$ using different methods for rectangular silicon WBGs with different $\Delta W$. The results are plotted in Fig. 11, where the experimental results of the gratings fabricated by electron-beam lithography at Applied Nanotools Inc. [45] are also included. We can find that the obtained $\kappa$ by the $\Delta n_{\text{eff}}$ eigenmode approach is considerably larger than those of the experiments. For the CMT based perturbation analysis, the results are relatively accurate when $\Delta W$ is smaller than 40 nm, i.e., when the coupling is not too strong and the CMT assumption is satisfied. However, the results start to deviate significantly from the experimental values when $\Delta W$ is larger than 40 nm, as weak coupling condition breaks down. The results obtained by the FDTD band-structure method, however, agree well with the experimental values. This suggests that the band structure approach is a more reliable and accurate method compared with others to assess $\kappa$ for WBGs.

### 2.6 Impact of manufacturing issues on the spectral performance

Spectral response of WBGs is quite sensitive to manufacturing induced imperfections. Fabrication imperfections include wafer thickness and waveguide width variability, which can lead to non-uniform refractive index distributions along the waveguide and thus introduce chirp along the grating [46]. It has been studied that the waveguide parameters like height, etching depth etc. change considerably from region-to-region within a chip [46,47], which adversely impacts the spectral performance of the WBGs, especially for longer gratings with several millimeters length. An approach to alleviate this issue is to translate the long WBG into a much more compact spiral shape. Due to the high compactness of spiral WBGs, the impact of chip variability can be mitigated considerably; allowing for the spectral response to be more precisely controlled. The implementation and performance of such

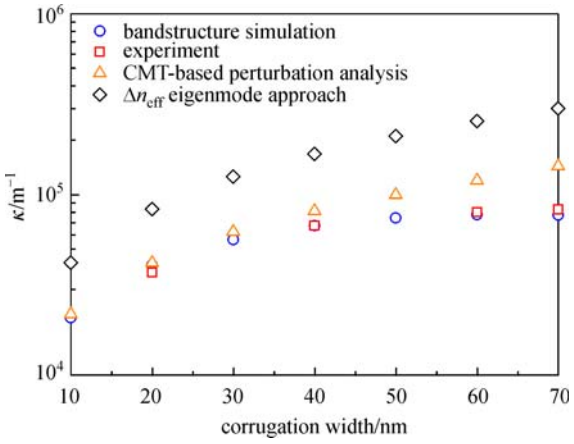


**Fig. 11** $\kappa$ versus corrugation width $\Delta W$ calculated by the different approaches, with the experimental values of the gratings fabricated by electron-beam lithography included for the comparison

spiral WBGs have been studied in Refs. [48–50]. Such highly compact WBGs are promising to achieve well-defined complex spectral response for various MWPs applications. Fabrication non-idealities also include corrugation width $\Delta W$ variability, which can not be precisely controlled due to limited lithography accuracy and resolution. Simulations are performed to give a rough estimate of how such parameter jitters can degrade the grating spectral performance. Random variations of $\Delta W$ with a Gaussian distribution are imposed on a grating with a bell-like apodization profile, and the transfer matrix method is used to calculate the spectral performances. Figure 12(a) plots the spectra when $\Delta W$ jitter with different standard deviations $\sigma$ is applied on the grating. It can be seen that the side-lobe suppression ratio is lower when $\sigma$ is higher, i.e., when the $\Delta W$ jitters effect is stronger. Figure 12 (b) compares the grating spectra between different grid sizes and thus different lithography resolutions for a fixed $\Delta W$ jitter. As expected, the spectral performance degrades when a larger grid size is involved. Also, by comparing the left and right plots in Fig. 12(b), one can notice that the grid size has a higher impact on the grating spectra when the jitter effect is stronger. These results clearly suggest that fabrication processes with a high accuracy and resolution is essential to acquire high-performance and well-controlled spectral responses for WBGs. Finally, waveguide roughness is also a factor that prevents from precisely tailoring target spectral responses on waveguide WBGs. For high index contrast waveguide, such as SOI waveguide, sidewall roughness can severely degrade the performance of long WBG, due to the high sensitivity of effective refractive index on the waveguide dimension [51]. A comprehensive study of the impact of this effect on IBG spectral responses can be found in Ref. [51]. It was also suggested in Refs. [28,30,46] that developing WBGs on a wider multi-mode waveguide can effectively alleviate the issue, and decrease the effect of sidewall roughness on WBGs by more than one order of magnitude.

## 3 Ultrafast optical signal processors

All-optical signal processing units, such as real time optical Fourier transformers, Hilbert transformers, ultrafast pulse shapers etc., are generally interesting for realization of ultrafast information processing sub-systems; in particular, these units serve as key building blocks for implementation of MWP devices and sub-systems [12]. In this section, we will review some of the work done in realization of these elements on an ultra compact on-chip integrated platform.

### 3.1 Real time optical Fourier transformers

The well known mathematical analogy between Fresnel diffraction of monochromatic optical beams and narrow-band dispersion of optical pulses is the foundation of the space-time duality theory [52]. The real-time Fourier

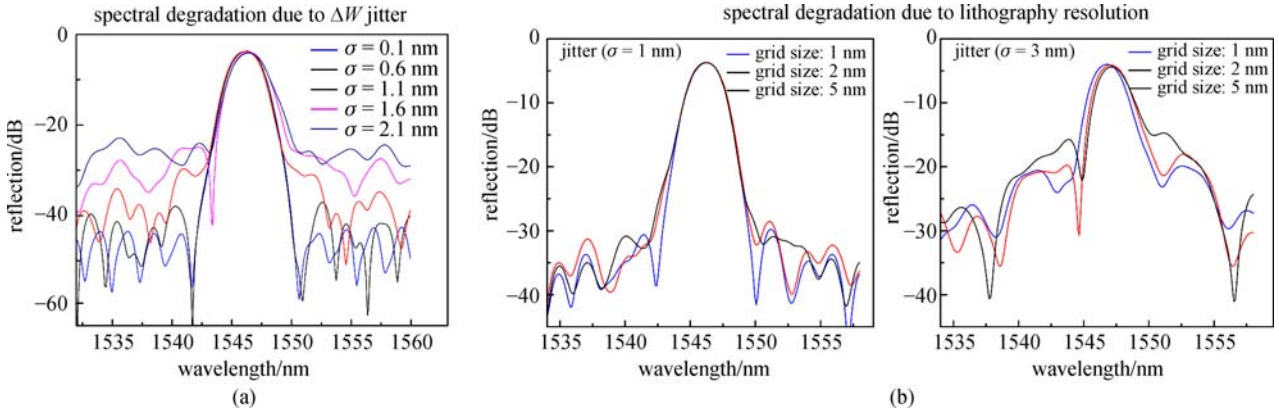


**Fig. 12** (a) Spectra of WBGs with different degrees of $\Delta W$ jitter effects applied. $\sigma$: standard deviations of $\Delta W$ variations. (b) Spectra of WBGs fabricated with different grid sizes when the $\sigma$ of $\Delta W$ jitter is (left) 1 nm and (right) 3 nm

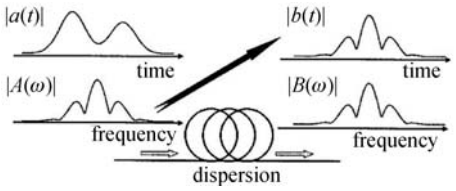


**Fig. 13** Frequency to time conversion using temporal chromatic dispersion. Reproduced from Ref. [53]

transformation by first-order chromatic dispersion is the temporal counter-part of the Fraunhofer or far-field free-space diffraction process. Through this process, a mapping of the energy spectrum of the input optical pulse (signal under test) to the time axis is possible i.e., frequency-to-time mapping [52], as shown in Fig. 13. This is simply induced by linear propagation of the optical waveform of interest through a transparent medium providing a large group-velocity dispersion (GVD), in which the group delay of the system varies in a linear fashion with respect to frequency [54]. The process has been employed for many important applications, such as real-time optical spectrum measurements [55,56], temporal magnification of broad-band waveforms [57], high-frequency arbitrary microwave waveform generation [58], real-time spectroscopy [59], etc. The first integrated real-time Fourier transformer based on a linearly chirped waveguide Bragg grating (LCWBG) on silica glass was demonstrated in Ref. [21]. A LCWBG is a special kind of waveguide grating where a linear chirp is introduced in the grating period along the device length to achieve the desired linear GVD [60]. The grating used in Ref. [21] was operated in reflection mode, with a frequency band-width of ~1.25 THz (~10 nm), and could process temporal waveforms as long as 20 ps.

*Experimental results*

The LCWBGs were laser written in fused silica glass using an externally modulated femtosecond laser. The device had a reflectivity wavelength bandwidth of approximately 10 nm, centered at 1550 nm. Fourier transform spectral interferometry (FTSI) was used to measure both the intensity and phase of the reflected fast waveform [61]. A tunable passively mode-locked fiber laser generating nearly transform-limited Gaussian pulses was used to generate the input pulses. Switchable optical band-pass filters (OBFs) were used to limit the pulse spectrum. In Fig. 14, the experimental response of the demonstrated real-time Fourier transformer is shown for input waveforms consisting of two consecutive short pulses. Figures 14(a) and 14(b) display the spectra of the incident and reflected signals when a 3 nm OBF was used, together with the scaled oscilloscope traces of the temporal reflected signals for the cases when the two incident pulses were in phase and π-phase shifted, respectively. The measured spectral bandwidths correspond to transform limited pulses with a time duration of 700 fs. In Fig. 14(c), the spectrum of the reflected signal together with its scaled temporal waveform trace for a pair of in-phase incident pulses is shown. In this latest case, the temporal pulse duration was fixed to be approximately 1.2 ps, and the output temporal duration was approximately 150 ps. The phase of the reflected signal reconstructed through FTSI is shown in Fig. 14(d), retrieving a quadratic phase variation that is very close to that expected from the dispersion characteristics of the LCWBG device. The measured dispersion (~34.8 ps/nm) is sufficient to perform accurate frequency-to-time mapping of waveforms as long as ~20 ps.

### 3.2 Real time Hilbert transformers

In applications such as radar, communication systems, image processing, computing, and networking, an important signal processing operation is temporal Hilbert transformation. A temporal Hilbert transformer (HT) is an all-pass filter providing a discrete phase shift of π (integer HT) or a fraction of π (fractional HT) at the filter's central frequency. The transfer function of a fractional Hilbert transformer (FHT) is given by the expression

$$H_{\mathrm{FHT}}(\omega)=\begin{cases}\exp\left(\mathrm{j}P\dfrac{\pi}{2}\right), & \omega<0,\\ 0, & \omega=0,\\ \exp\left(-\mathrm{j}P\dfrac{\pi}{2}\right), & \omega>0,\end{cases} \tag{8}$$

where $j$ is the imaginary unit, $\omega=\omega_{\mathrm{opt}}-\omega_0$, $\omega_{\mathrm{opt}}$ represents the optical frequency variable, $\omega_0$ is the carrier frequency of the optical signal to be processed, and $P$ is the fractional order of the FHT. $P$ can be any rational number between 0 and 2; $P=1$ in case of an integer HT.

#### 3.2.1 On chip THz bandwidth fractional Hilbert transformer (FHT)

The work in Ref. [18] reported the realization of an integrated photonic fractional Hilbert transformer (FHT) fabricated through a standard CMOS photolithographic process, which is capable of efficiently processing optical pulses with THz bandwidths. The FHT was based on a very simple, uniform, and nonapodized phase-shifted waveguide Bragg grating (PS-WBG), where the fractional order can be chosen by design by simply engineering the effective index modulation $\delta n$. The resulting structure was also extremely compact compared with previous demonstrations, with a total grating length of only 65 μm.

The Hilbert transformer transfer function can be approximated by the response of a physical filter realized with a PS-WBG, operated in reflection, integrated in a SOI technology. The specific device demonstrated here was

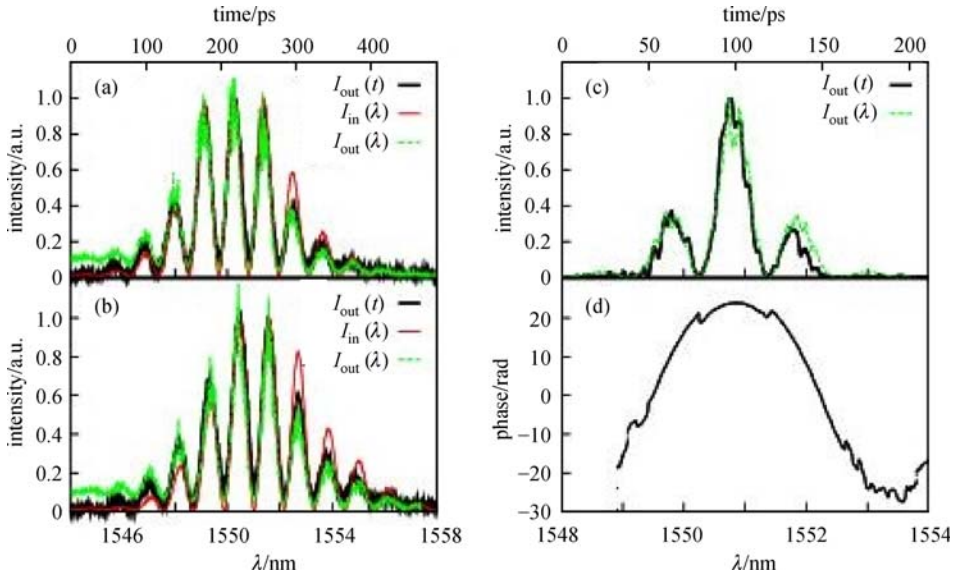


**Fig. 14** Incident (solid red curve) and reflected (dashed green curve) spectra superimposed on the scaled oscilloscope traces of the output temporal waveforms (solid black curve): (a) for in-phase incident pulses and (b) for π-phase-shifted incident pulses. (c) Spectrum (dashed green curve) and the scaled temporal waveform (solid black curve) of the reflected in-phase double pulse signal reconstructed through Fourier transform spectral interferometry (FTSI). (d) Phase of the reflected signal reconstructed through FTSI. Reproduced from Ref. [21]

designed in a 220 nm thick × 500 nm wide silicon strip waveguide and it featured 100 nm sidewall corrugations with a period of 325 nm. The phase shift was introduced in the middle of the grating structure, with 100 grating periods on either side of the phase shift, for a total length of the PS-WBG of approximately 65 μm. Anoptical vector analyzer (OVA) was employed to characterize the optical transfer function in reflection of the realized PS-WBG. The measured magnitude and phase responses of the grating are shown in Fig. 15 in comparison with the transfer function of an ideal FHT. The realized filter approximates very well the ideal response, with an instantaneous bandwidth as wide as 16.8 nm (2.14 THz) and a phase transition of 1.5π radians (equivalent to a fractional order of 1.5) around the central frequency.

In order to characterize the time-domain response of the device to a transform-limited Gaussian-shaped probe pulse, FTSI was employed. Experiments were performed for pulses of various durations, between 1.5 ps (≈300 GHz bandwidth) and 15 ps (≈30 GHz bandwidth), and the measured time domain pulses were compared with the ideal responses. Two examples are presented in Fig. 16, for a pulse duration of (a) 4 ps and (b) 1.5 ps at full width at half-maximum (FWHM), showing a root mean square error (RMSE) of 2.44% and 0.49%, respectively.

### 3.2.2 Silicon laterally apodized waveguide Bragg gratings (WBGs) based Hilbert transformers

High-performance integrated photonic fractional and integer-order HTs fabricated through a standard single-etch electron-beam (E-beam) lithography process were designed and demonstrated in Ref. [16]. The fabricated devices were based on sub-millimeter long, laterally apodized WBGs on a SOI platform. This design uses two individual superposed gratings, as shown in Fig. 17. Section 2.3 provides the details of such a WBG design. This approach offers increased tolerance to fabrication errors, so that it allows the control of grating apodization with very high precision over a large dynamic range, enabling, for instance, the realization of an integer HT with a processing bandwidth as large as ~750 GHz and a time-bandwidth product (TBP) above 20. TBP is a principal figure merit of a device's temporal/spectral response, and is defined as the ratio between the maximum operation bandwidth and the minimum signal bandwidth that can be processed with a prescribed precision. Here, the grating corrugations were defined on the side-walls of a 220 nm thick × 500 nm wide single-mode silicon strip waveguide fabricated on a SOI wafer. As the first step, Lumerical Mode Solutions was used to extract the effective refractive index of the waveguides. Then, the transfer matrix method was implemented to model the WBG device. Assuming a fixed corrugation depth, the target grating apodization was transferred to the lateral shift between the relevant periods of the device according to the following equation

$$\Delta n_0 = n_0 \cos(\pi \Delta L / \Lambda), \tag{9}$$

where $n_0$ is the effective-index modulation for the WBG device with no misalignment ($\Delta L = 0$). The grating period

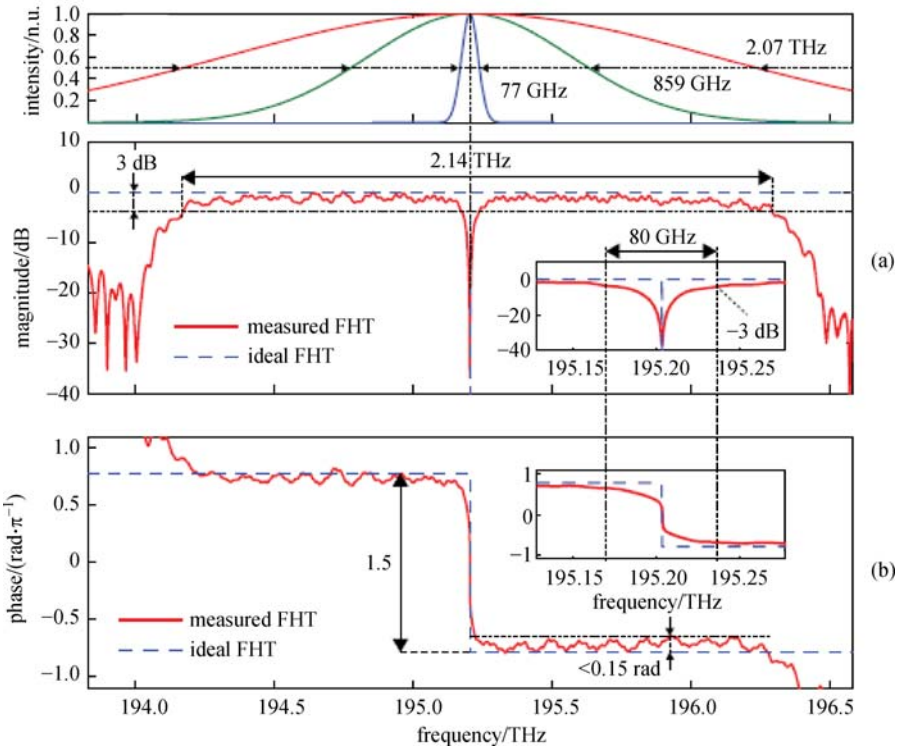


**Fig. 15** Measured reflection spectral response of the fabricated phase-shifted waveguide Bragg grating (PS-WBG) compared with the ideal fractional Hilbert transformer (FHT) response in (a) magnitude and (b) phase. The top inset shows examples of Gaussian input pulse spectra. Reproduced from Ref. [18]

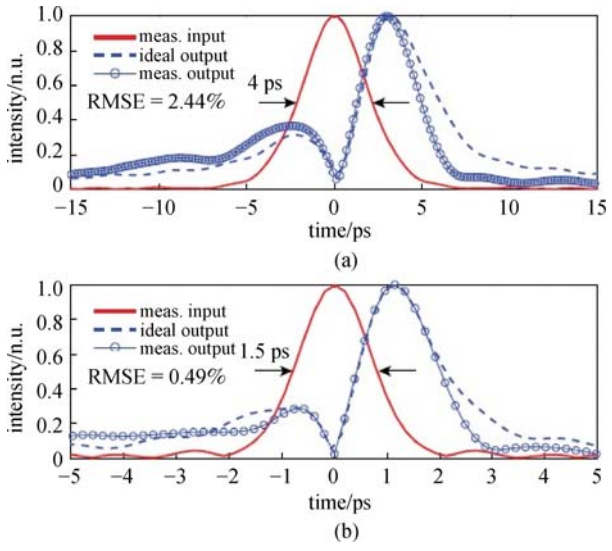


**Fig. 16** Time-domain experimental testing results. The figure shows the measured input pulse (solid line), simulated output pulse obtained by filtering the measured input pulse with an ideal Hilbert transformer (dashed line), and actual output pulse measured using Fourier transform spectral interferometry (FTSI) (circled line), for input pulses with full width at half-maximum (FWHM) durations of (a) 4 ps and (b) 1.5 ps. Reproduced from Ref. [18]

(Λ) was considered to be 318 nm, with a duty cycle of 50%, to achieve operation around a telecommunication wavelength (~1555 nm). The misalignment (Δ$L$) was varied from 0 to 159 nm (Λ/2). A schematic of the apodized WBG is shown in Fig. 17.

*Experimental results*

The spectral amplitude and phase responses of the device were measured using an optical vector analyzer; the simulation and experimental results are shown in Figs. 18 (a) and 18(b), 18(d) and 18(e) respectively. The TBP of each evaluated device is estimated as the ratio of the longest input pulse time-width to the shortest pulse time-width that provides a minimum prescribed cross-correlation coefficient between the output temporal waveform and the ideal expected one (89% in the evaluations reported here). Cross-correlation coefficient, is a measurement of similarity between the obtained output temporal waveform and the expected one assuming an ideal performance of the signal-processing device. According to Figs. 18(g) and 18 (h), doubling the number of grating period results in approximately a two-fold improvement in the devices TBP, from nearly 12 to above 20. Figures 18(j) and 18(k) show examples of the temporal response of the measured device under test (DUT) to a 4 ps FWHM sample Gaussian pulse, compared with the ideal HT response. The second experimentally tested example was a fractional order HT with $P$ = 1.5, designed using a similar grating structure, but with 2000 periods of 324 nm and a larger corrugation depth of 10 nm. The corresponding simulation, experi-

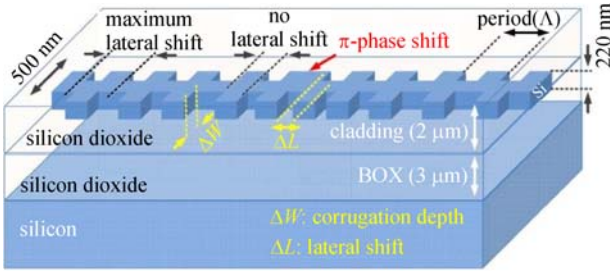


**Fig. 17** Schematic of a laterally apodized waveguide Bragg grating (WBG). Reproduced from Ref. [16]

mental, TBP and temporal response results are shown in Figs. 18(c), 18(f), 18(i) and 18(l) respectively.

### 3.3 Ultrafast pulse shaping

The ability to engineer ultrashort-pulse waveforms optimized for specific applications has had a significant impact in fields as diverse as ultrafast spectroscopy, nonlinear fiber optics and fiber communications, among many others. Ultrafast pulse shaping methods are based on the well-known concept of linear time-invariant filters [62]. Linear filtering can be described in either the time or the frequency domain, as depicted in Fig. 19. In the time domain, the filter is characterized by an impulse response function $h(t)$. The output of the filter $e_{out}(t)$ in response to an input pulse $e_{in}(t)$ is given by the convolution of $e_{in}(t)$ and $h(t)$. In the frequency domain, the filter is characterized by its frequency response $H(\omega)$. The output of the linear filter $E_{out}(\omega)$ is the product of the input signal $E_{in}(\omega)$ and the frequency response $H(\omega)$. For a delta function input pulse, the input spectrum $E_{in}(\omega)$ is equal to unity, and the output spectrum is equal to the frequency response of the filter. Therefore, generation of a desired output waveform can be accomplished by implementing a filter with the required frequency response. It is to be understood that both short-period (Bragg) and long-period grating devices have proven challenging to fabricate in integrated-waveguide configurations, particularly if they are intended to synthesize complex waveforms, e.g., with high resolutions, below the sub-picosecond regime, over long durations, above a few picoseconds [63,64]. Additionally, Bragg grating devices need to be operated in reflection and it would be also difficult to add reconfigurability in these structures, e.g., through the integration of high-resolution thermo/electro-optical controllers, due to the nanometer-scale of the grating features. In the following sections, we look into the implementation of compact Mach-Zehdner interferometers (MZIs) and directional coupler based filters to achieve the desired pulse shaping operations.

#### 3.3.1 Ultra short pulse generation using on-chip Mach-Zehdner interferometers (MZIs)

An on-chip (CMOS)-compatible Mach-Zehdner interferometer (MZI) was used for flat-top pulse generation by linearly re-shaping an input Gaussian-like optical pulse [65]. A typical MZI works by splitting light equally into two arms of the interferometer and then recombining the two beams. Depending on the optical path length

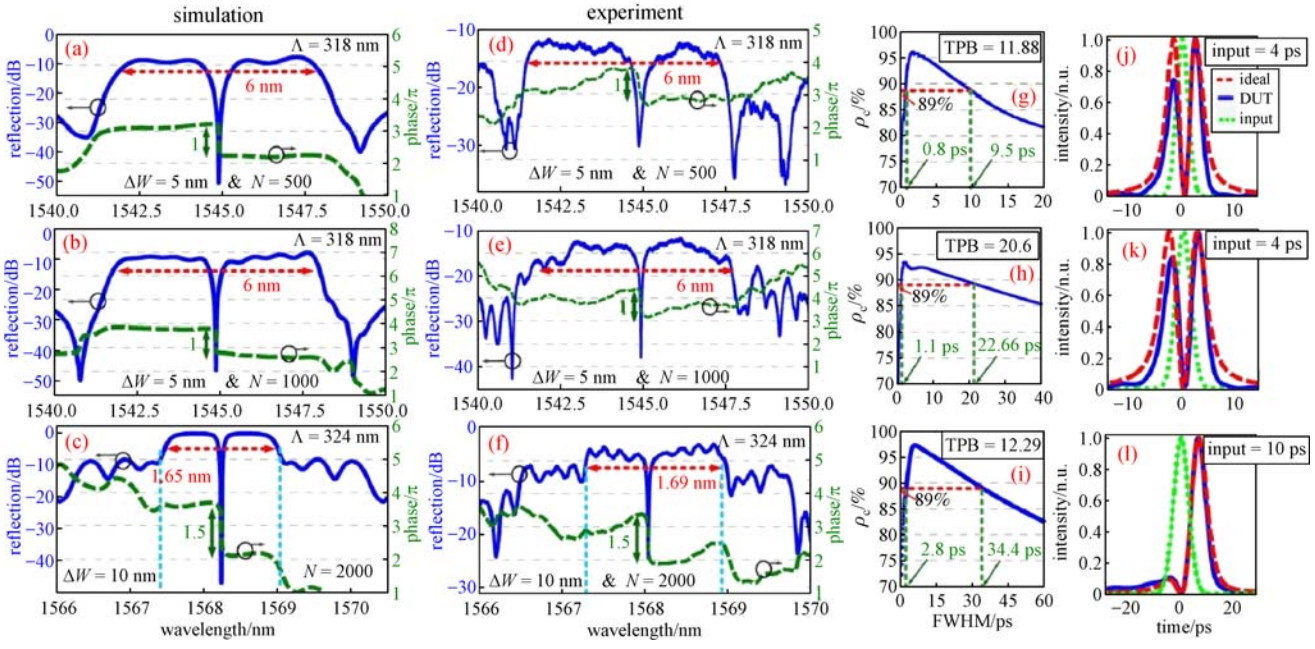


**Fig. 18** (a)–(c) Simulated and (d)–(f) measured amplitude and phase spectral responses, (g)–(i) cross-correlation coefficients, and (j)–(l) comparison between the temporal responses of ideal HTs with the response from the fabricated devices to different Gaussian pulses for the integer (two top rows) and fractional (last row) photonic HTs. Reproduced from Ref. [16]

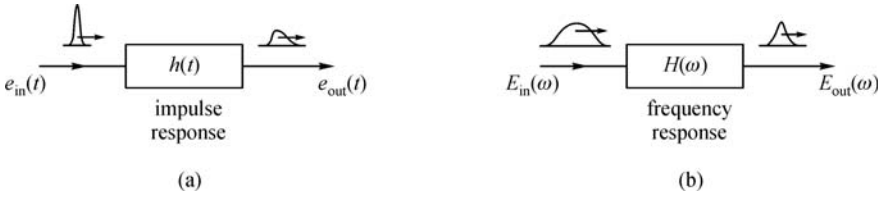


**Fig. 19** Pulse shaping by linear filtering: (a) time-domain view; (b) frequency-domain view

difference between the two arms, fringes as a function of wavelength are observed. These fringes correspond to the constructive/deconstructive interference. By simple linear propagation through the same integrated device, a 7.8-ps Gaussian-like pulse was reshaped into 17.1-ps and 20.0-ps flat-top pulses using two different linear filtering schemes. In addition, the capability of this MZI to implement the generation of a Hermite-Gaussian pulse with duration of a few picoseconds was also demonstrated.

*Experimental results*

The device was based on high-index contrast (4%) silica-on-silicon waveguides of 22 μm$^2$ cross section fabricated using a combination of plasma-enhanced chemical vapour deposition, photolithography and dry etching processes. Figure 20(a)-(i) shows the spectra of the ultrashort pulse before and after propagation through the MZI. Since there is a π phase shift at each notch wavelength, the desired sinc-like field spectrum was practically achieved. In this case, the device FSR of 100 GHz imposes a time width of ~10-ps for the flat-top region of the generated pulse. The time-domain intensity profiles of the input pulse, the measured output pulse and the simulated ideal output are shown in Fig. 20(a)-(ii). As anticipated, the input 7.8-ps Gaussian-like optical pulse was re-shaped into a 17.1-ps (FWHM) flat-top pulse.

In a different experiment aimed at generation of a Hermite-Gaussian pulse waveform, a nearly transform-limited Gaussian-like optical pulse with a time-width of 11-ps was directed into the integrated MZI. The carrier wavelength of the optical pulse was tuned to match the notch wavelength of the MZI, i.e., to operate the MZI as an optical differentiator. The spectra of the optical pulse before and after the MZI are shown in Fig. 20(b)-(i). The temporal waveform before and after the MZI was measured using a FTSI setup with the results shown in Fig. 20(b)-(ii). The measured time-domain output pulse agrees well with the simulated ideal one (numerical derivative of the input Gaussian pulse), including the anticipated discrete π phase shift between the two consecutive Gaussian-like lobes.

### 3.3.2 Sub-picosecond optical pulse shaping in silicon based on discrete space-to-time mapping (STM)

Discrete space-time mapping (STM) is a technique where the discrete amplitude and phase apodization profile of a given device can be directly mapped into its output temporal response. Consider a structure of cascaded directional couplers as shown in Fig. 21; the proposed design is based on forward coupling between a main waveguide and a bus waveguide in which the coupling is controlled in a discrete fashion through standard codirectional couplers. In practice, the vertical spacing between these waveguides (coupling gap) or their length (coupling length) could be tuned to achieve different coupling ratios, see Fig. 21(c). Additionally, the discrete phase profile also can be tuned by adjusting the relative optical path length difference between the bus and main waveguides connecting the upper and lower ports of consecutive couplers, respectively (Fig. 21(b)). Experimental demonstration of discrete STM for optical pulse shaping and coding on a SOI chip platform was presented in Ref. [66], based on the design methodology first introduced in Ref. [67], successfully achieving the synthesis of both amplitude and phase temporal shapes, e.g., flat-top pulses and phase-coded pulse trains, with resolutions ranging from the femtosecond to the picosecond regime.

*Experimental results*

The first experimental target waveforms were 1.25 and 3 ps FWHM flat-top pulses synthesized from an input 54 fs optical Gaussian pulse, which was directly generated from a passively mode- locked fiber laser with a repetition rate of 16.8 MHz. 10 or 20 couplers (for 1.25 or 3 ps pulses, respectively) with identical coupling coefficients of ~0.001 were connected in series through 11.5 μm relative-delay lines, corresponding to a sampling time of $\tau \approx 174$ fs. A schematic of the pulse shaping device is shown in Fig. 21. The reported devices were made using 220 nm thick × 500 nm wide silicon-strip single-mode waveguides, fabricated on a SOI wafer.

Direct time-domain characterization of the output, synthesized waveforms was carried out using FTSI with the input optical pulse serving as the reference. The results shown in Fig. 22 confirm that the obtained transform-limited flat-top pulses are of very high quality, having successfully synthesized a remarkable number of spectral sidelobes.In addition to FTSI, OVA was used to measure the amplitude temporal response and power spectral response of each of the fabricated devices. An additional femtosecond-regime flat-top pulse synthesis experiment

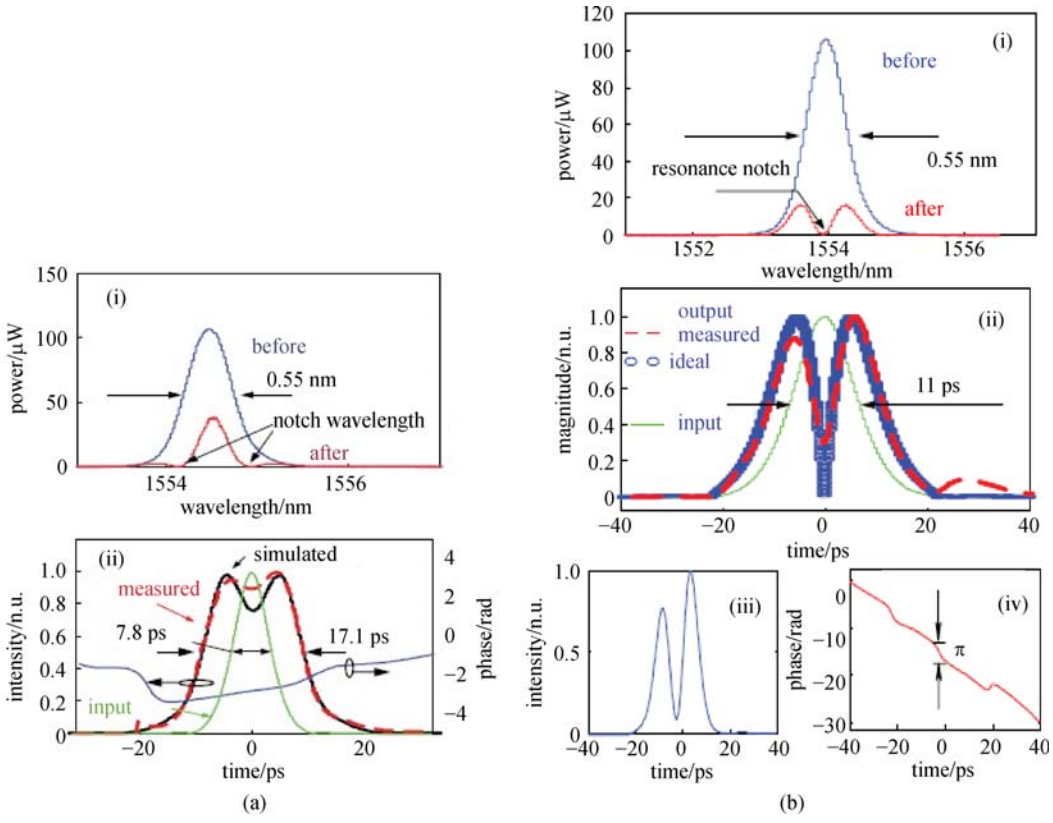


**Fig. 20** (a) (i) Spectra of the ultrashort pulse of 7.8 ps pulse width before and after propagation through the fabricated Mach-Zehdner interferometer (MZI) when the pulse carrier wavelength matches one of the MZIs peak transmission wavelengths. (ii) Time-domain intensity profiles of the input pulse, the measured output pulse, and the simulated ideal output. Phase profile of the measured output pulse is also shown. (b) (i) Spectra of the ultrashort pulse of 11 ps pulse width before and after propagation through the fabricated MZI when the pulse carrier wavelength matches one of the MZIs notch transmission wavelengths. (ii) Time-domain intensity profiles of the input pulse, the measured output pulse, and the simulated ideal output. (iii) and (iv) Intensity and phase profiles of the measured output pulse. Reproduced from Ref. [65]

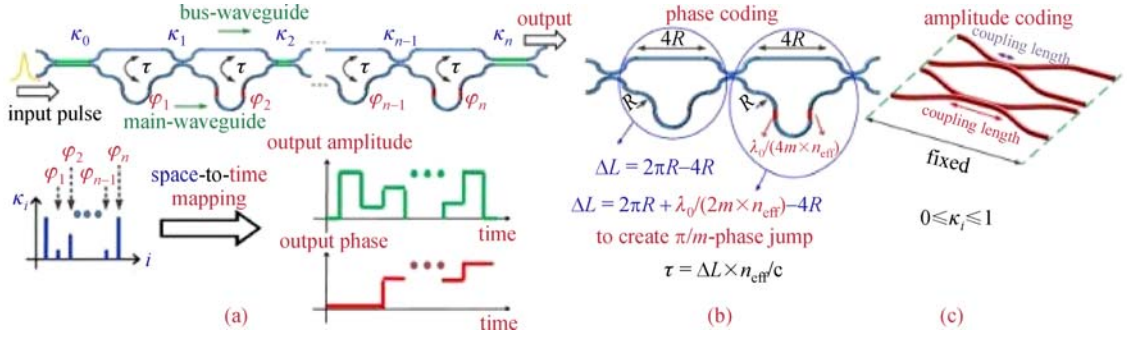


**Fig. 21** (a) Schematic of the proposed pulse shaping device and its principle of operation. (b) Phase coding by tuning the waveguide length in the differential delay lines. (c) Amplitude coding by tuning the coupling length. Reproduced from Ref. [66]

was reported in Fig. 22. In this case, five identical couplers were cascaded with a relative length difference of 6.8 μm, corresponding to a time delay of $\tau \approx 100$ fs.

The demonstrated devices were fully passive so that no additional strategies have been used to tune the devices parameters to achieve the target waveforms. This design approach could be adapted for application over a wide range of temporal resolutions, from the sub-picosecond to the sub-nanosecond regime, and it should enable the synthesis of relatively complex (high TBP) temporal waveforms.

Development of design strategies to extend the operation range of the discrete STM approach for synthesizing pulse waveforms with significantly longer temporal durations was carried out in Ref. [68]. In particular, experimental demonstration of the re-shaping of a

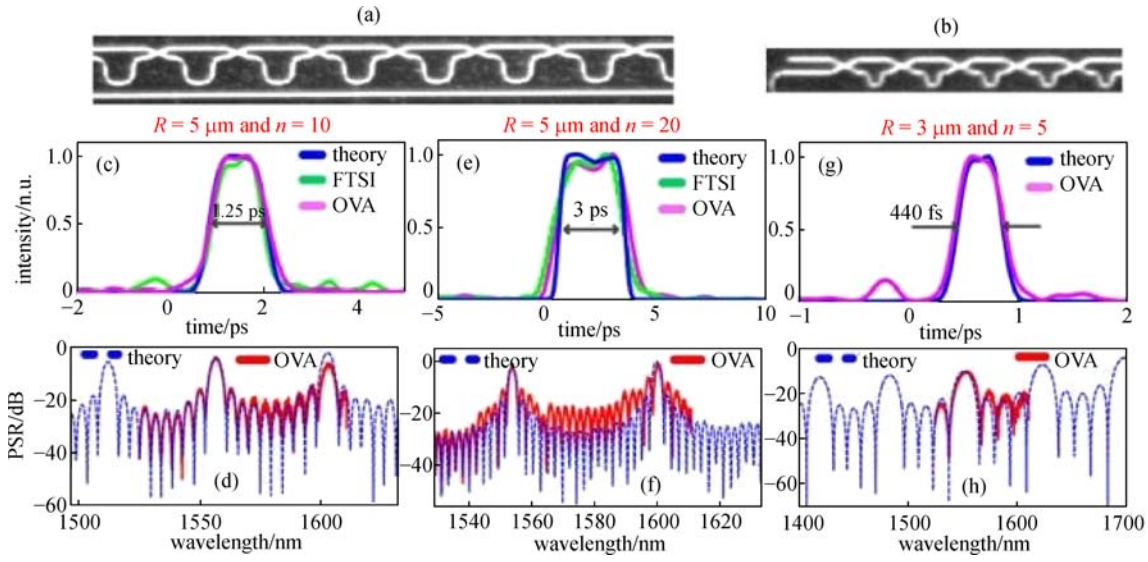


**Fig. 22** Micrographs taken using a camera mounted on a microscope, from part of the fabricated devices with [(a) and (b), respectively] $R = 5$ μm and 3 μm; (c) and (d), respectively, the simulated and measured amplitude temporal response and power spectral response (PSR) of a device consisting of $n = 10$ identical cascaded couplers; (e) and (f), respectively, $n = 20$ identical cascaded couplers; and (g) and (h), respectively, $n = 5$ identical cascaded couplers with a shorter delay difference. Reproduced from Ref. [66]

picosecond Gaussian optical pulse into 1) high-quality ~70 ps flat-top pulses and 2) a 40 ps 16-QAM bit pattern, using all-passive devices in SOI technology (with no post-fabrication tuning process involved) was reported. Readers are directed to Ref. [68] for detailed results.

## 4 Integrated microwave photonics (IMWP)

Microwave photonics (MWP) is a well-established field of research where radio frequency signals are generated, processed, transported and analyzed using photonic techniques [8,9]. This technology enables various functionalities which are generally not feasible by means of electronic techniques alone, such as, high purity terahertz signal generation [4,5], transport of millimeter wave signals over hundreds of kilometers scale distances with very low attenuation [69]; ultra-narrow (MHz scale) microwave notch filters with ultra-broad tuning range (tens of GHz) [70], and more. In recent years, the progress in integrated optics has been leveraged to provide flexible, robust, low cost MWP signal processors realized on a compact chip, giving birth to the field of integrated microwave photonics (IMWP) [10]. Recent demonstrations showed a fully-integrated IMWP processor, where all active and passive optoelectronic components are integrated in the same chip [71]. Moreover, integrated optical signal processors for microwave signals that are fully reconfigurable to implement multiple signal processing functionalities, including finite and infinite impulse response filters, have also been reported [72,73].

The concept of a reconfigurable photonic processor is based on the fact that a large number of complex signal processing functions can be implemented based on a few basic operations, particularly splitting/combining, tunable true-time delay (TTD) and phase shifting (PS). To realize complex processors on a compact footprint, it is therefore important that these basic operations can be performed with high accuracy and using compact structures. In the following sub-sections we will discuss some of these functionalities, i.e., TTD, PS, etc., demonstrated using ultra compact WBG elements on the SOI platform. Owing to their compact size (only hundreds of micrometers long) and ultra broad bandwidth ( > 10 s GHz up to THz), these devices show a strong potential for applications to IMWP signal processing. They have been applied to multiple applications, such as reconfigurable optical filtering of microwave signals, optical control of phased array antennas, microwave frequency measurement, and more [17,20].

### 4.1 On-chip programmable phase shifters and true-time delay (TTD) unit

An extremely compact (≈130 μm long) and simple device, integrated on a silicon platform, which can be reconfigured to operate both as a continuously true-time delay (TTD) and as a phase shifting (PS) over different GHz-level bandwidths was demonstrated in Refs. [19,20]. The device was based on a single uniform WBG with two phase-shift sections, operated in reflection. This architecture gives a sharp phase shift that can be exploited to generate either PS or TTD on the RF signal.

As stated, a filter with the desired intensity and phase

responses for implementing a tunable TTD and PS can be realized using a dual-phase-shifted waveguide Bragg grating (DPS-WBG) integrated in an SOI waveguide. The grating was designed in a 220 nm thick × 500 nm wide silicon strip waveguide. The gratings are formed with 100 nm sidewall corrugations, corresponding to an effective index modulation, $\delta n \approx 0.0042$, with a grating period of 325 nm. Two phase-shifts were introduced in the device. The number of grating periods was 100 on both grating ends, and 200 between the two PS sections.

*Experimental results*

The nearly flat response of the DPS-WBG (ripple < 2.5 dB) over a band of more than 1.7 THz, with a shallow notch (approx. 2.3 dB) around the center of the reflection band can be used to implement the desired RF photonics signal processing functions, see Fig. 23(a). The notch corresponds to a sharp transition in the phase response (approx. 300° over 80 GHz).

DPS-WBG response can directly implement an ultra broadband PS. Considering an optical single-sideband with full carrier (OSSB + C) modulation scheme, by adjusting the optical carrier wavelength with respect to the resonance frequency of the DPS-WBG, it is possible to provide the desired amount of phase shift $\phi_c$ to the carrier only, while keeping the sideband phase unaffected, as shown in Fig. 23(b). The same device can be also employed as a microwave TTD with an instantaneous bandwidth of approximately 10 GHz. By simply varying the position of the carrier with respect to the resonance frequency, the phase transition around resonance of the DPS-WBG can be used to approximate a linear phase response with different slopes (Fig. 23(c)), implementing a tunable TTD line.

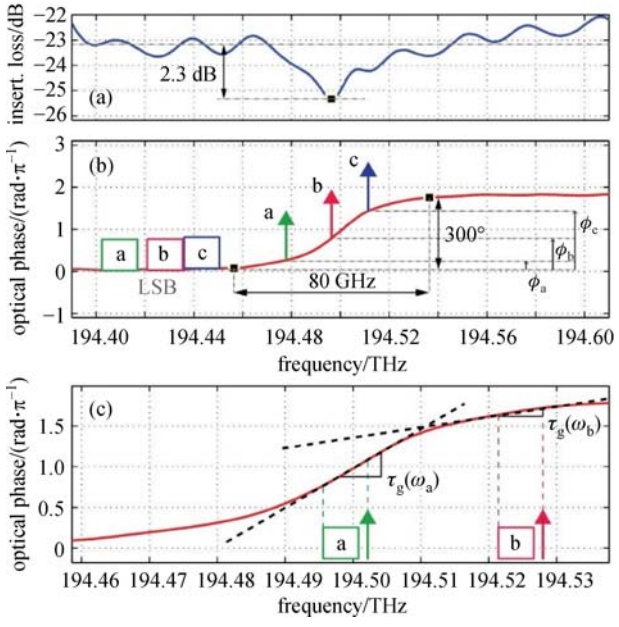


**Fig. 23** Dual-phase-shifted waveguide Bragg grating (DPS-WBG) magnitude response (a), operation as phase shifting (PS) (b), and true-time delay (TTD) (c). Reproduced from Ref. [19]

Figure 24(a) shows the experimentally obtained magnitude and phase response of the device for different carrier wavelengths, which shows the possibility to induce a continuously tunable and broadband RF phase shift of approximately 160°, over an instantaneous bandwidth between approximately 22 and 29 GHz.

Figure 24(b) presents results corresponding to the TTD operation, showing continuous tunability of the delay response in the range 0 – 19.4 ps, over an instantaneous microwave-signal bandwidth of approximately 1 to 10 GHz, as induced by simply tuning the optical carrier wavelength.

### 4.2 Real time radio frequency (RF) identification system

Real time frequency identification systems are useful for a wide range of applications in modern biomedical instrumentation, astronomy, electronic countermeasure (ECM), radar warning and electronic intelligence systems etc. For many electronic warfare applications, the measurement of frequency is one task that can be performed more efficiently by a specialized instantaneous frequency measurement (IFM) receiver. Most of the currently available systems rely on high optical power (> 100 mW) and/or are limited in usable bandwidth (~10 GHz). Additionally, these systems are typically bulky and expensive. To this effect, the real time frequency identification system demonstrated in Ref. [17] in an ultra compact fully linear CMOS compatible silicon on insulator platform has an operable bandwidth of up to 30 GHz.

#### 4.2.1 Operating principle

In this work, a single, very simple and compact optical WBG filter on-chip was employed. The filter was realized using a phase shifted WBG (PS-WBG) in CMOS compatible silicon on insulator platform. Figure 25 shows the schematic of the 65 μm long PS-WBG filter, where the input and output of the filter were accessed using grating assisted couplers. A Y-branch was used to access both the transmission and the reflection responses of the filter. The grating was simultaneously operated in transmission and reflection to provide two separate frequency responses. The simulated and measured responses for both transmission and reflection ports are shown in Figs. 26(a) and 26(b). The functions $|s_{21,TX}|$ and $|s_{21,RX}|$, in linear scale, indicate the amplitude (voltage) ratios between the transmission and reflection RF outputs, respectively, and the RF input. These are shown in Fig. 26 (e). Based on these responses, an amplitude comparison function (ACF) is defined as detailed in Eq. (10).

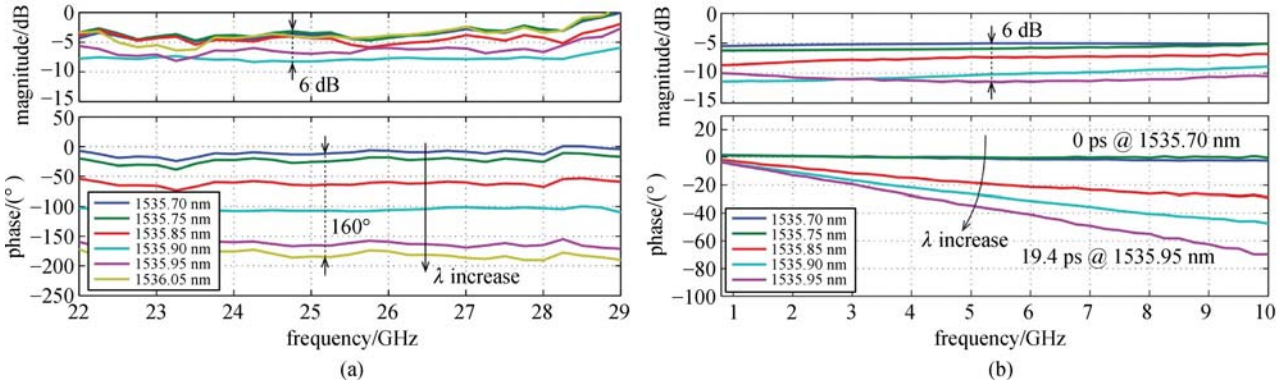


**Fig. 24** (a) Complex (magnitude and phase) radio frequency (RF) response for different phase shift values. (b) Complex (magnitude and phase) RF response for different true time delay values. Reproduced from Ref. [19]

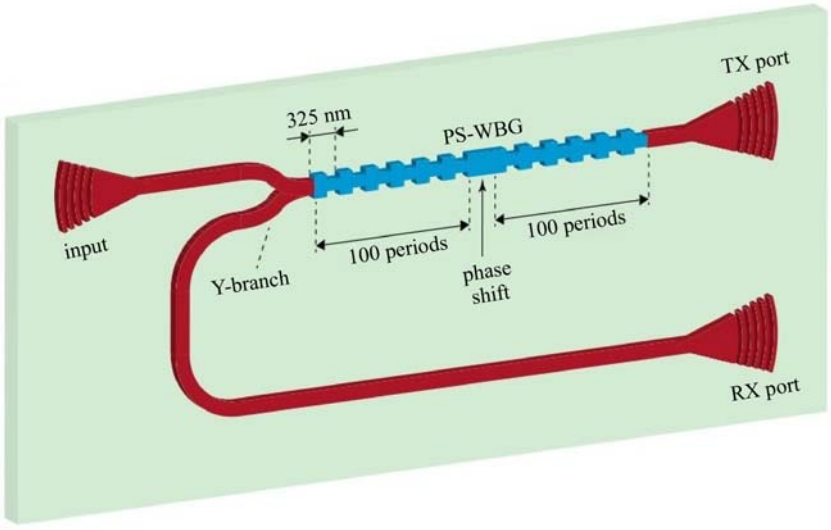


**Fig. 25** Schematic of the silicon WBG (PS-WBG) employed as a linear-optics frequency discriminator. TX port: transmission port; RX port: reflection port. Reproduced from Ref. [17]

$$\mathrm{ACF}(\omega)=\frac{P_{\mathrm{TX}}(\omega)}{P_{\mathrm{RX}}(\omega)}=\frac{|S_{21,\mathrm{TX}}|^2}{|S_{21,\mathrm{RX}}|^2}. \tag{10}$$

The microwave frequency to be determined is mapped to the corresponding microwave power by this ACF.

### 4.2.2 Experimental demonstration

An input continuous wave (CW) from a tunable laser was modulated with the RF signal under test (generated using a VNA) using a Mach Zehdner modulator. With proper biasing, an optical single sideband carrier (OSSB + C) was generated, which was subsequently amplified to compensate for losses. Via polarization controller and on chip grating couplers, the signal was fed to the WBG, which was partly transmitted and reflected by the grating following different paths and outputs from the transmission (TX) port and the reflection (RX) port, respectively. After amplification, high speed photodetectors (PDs) were used to detect the signal at the two ports. By inverting the ACF curve in Fig. 26(f), the power ratio in Eq. (10) can be used to estimate input frequency. The scatter plot in Fig. 27 shows the microwave frequency estimated using the IFM system versus the actual input frequency for each of the test tones, as well as the residual measurement error. The figure shows that the system is able to measure tones up to 32 GHz with a mean square error of 773 MHz. The degradation of noise figure of the photonic link leads to such uncertainty.

### 4.2.3 Dynamic frequency identification

It is imperative to look at the ability of the system to identify the frequency profile of rapidly varying RF signals

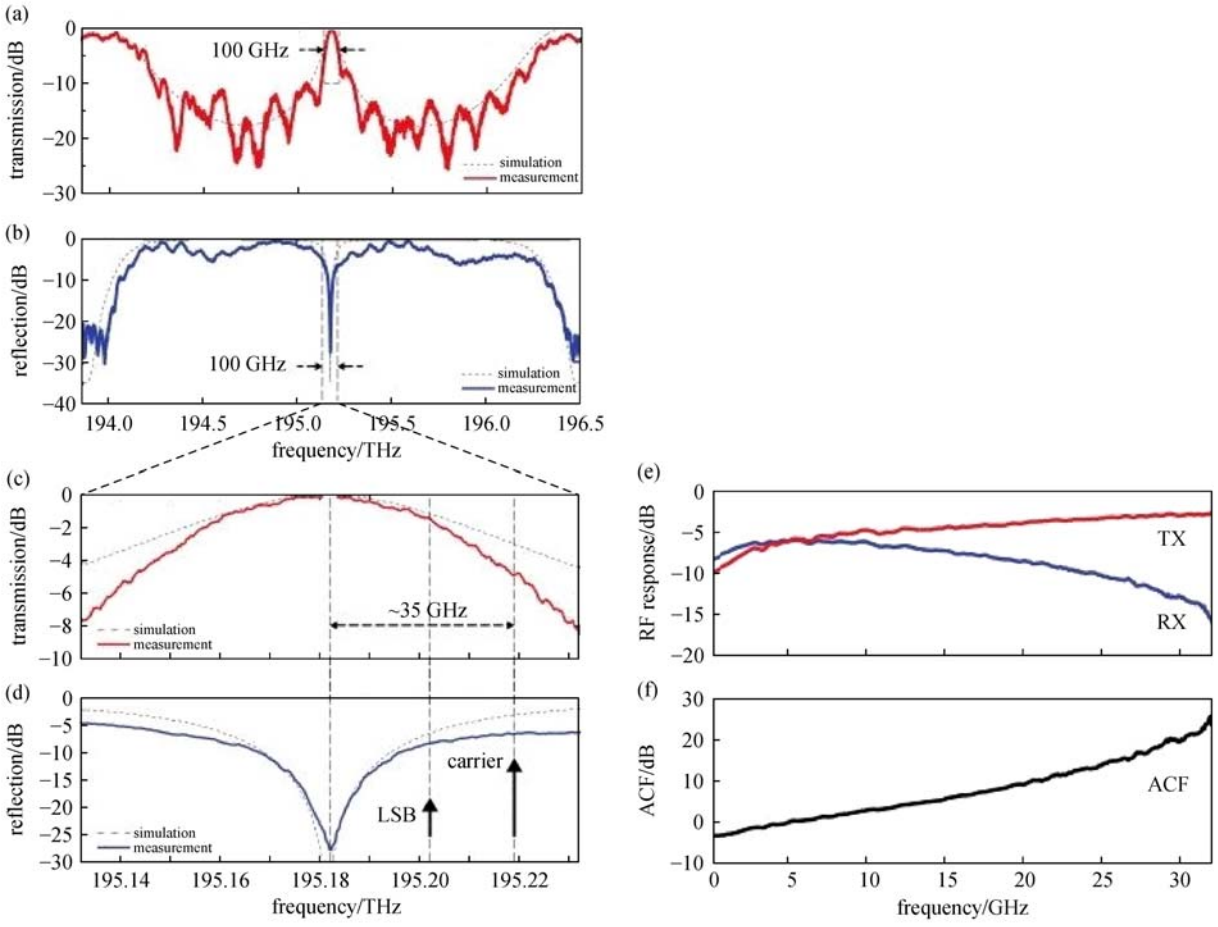


**Fig. 26** Simulated (dashed line) and measured (solid line; a) linear optical transmission and (b) reflection spectral responses of the phase-shifted waveguide Bragg grating (PS-WBG); (c) and (d) zoom with overlapped optical single sideband carrier (OSSB + C) spectrum. The optical responses are normalized to the maximum. (e) Radio frequency (RF) response of transmission (TX) and reflection (RX) ports; (f) ACF, obtained from Eq. (10). Reproduced from. [17]

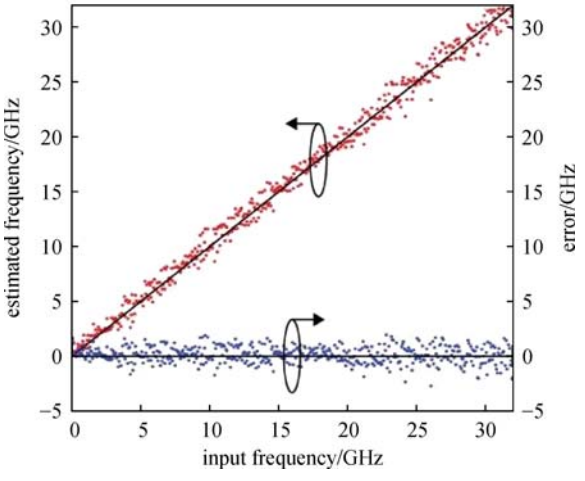


**Fig. 27** Estimated frequency (red dots) and corresponding error (blue dots). Reproduced from Ref. [17]

in a dynamic fashion. A frequency hopping signal (Fig. 28 (a)) generated from an arbitrary waveform generator (AWG) was fed to the input of the instantaneous frequency measurement (IFM) system. After processing through the IFM system, the average power of the signal $s(t)$ (Fig. 28 (b)) was extracted using a low pass filtering scheme (Fig. 28(c)). Inverse ACF was used to map the average power into the frequency profile. The resulting instantaneous frequency profile was extracted and shown in Fig. 28(d). Relatively low-frequency variations can be detected (300 MHz in this example) and the same frequency can be identified at different time slots in a highly reproducible manner. This is also shown in Fig. 28(d), where the frequency step sequence 0.6 – 1.5 – 3 GHz was chosen to appear twice, at the beginning and at the end of each burst. A direct comparison of the result in Fig. 28(d) with the spectrogram of the input signal in Fig. 28(e) shows that frequency identification is performed in an accurate

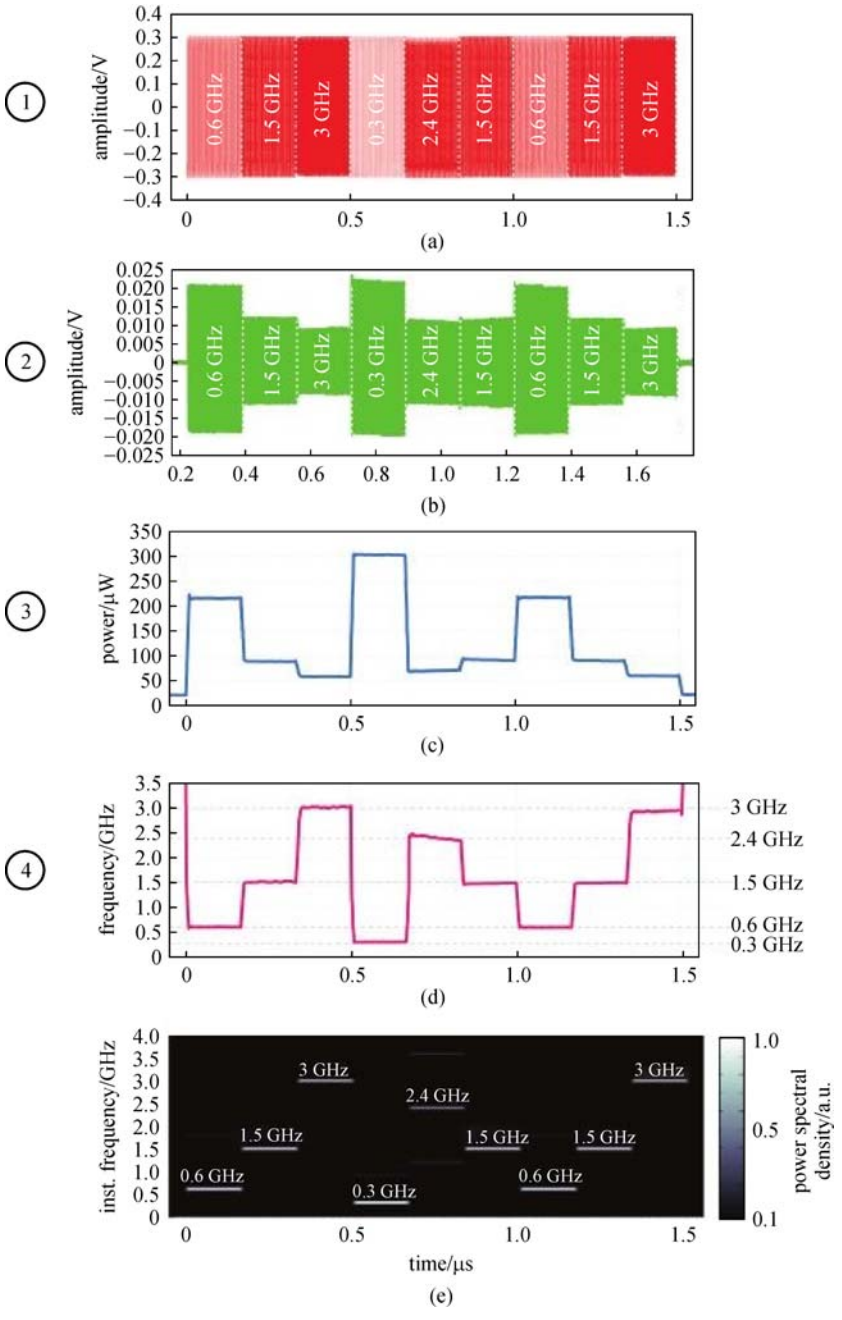


**Fig. 28** Experiment of dynamic frequency identification. (a) A radio frequency (RF) signal with unknown frequency content enters the photonic instantaneous frequency measurement (IFM) system. (b) Time-domain signal at the IFM output was amplitude-coded according to the time-varying frequency content of the input signal. (c) Instantaneous power was extracted by self-mixing and low-pass filtering. (d) Using the inverse amplitude comparison function (ACF), the RF frequency content was estimated in a dynamic manner. (e) Spectrogram of the frequency-hopping input sequence is shown for comparison. Reproduced from Ref. [17]

manner. Similar tests were performed to demonstrate the system's capability to identify higher frequency signals up to 12 GHz, only limited by the AWG specifications.

Due to ultra compact size, low power requirements, sub 100 ps latency, and CMOS fabrication compatibility, the IFM system based on silicon PS-WBG opens a solid path for realization of on chip integrated real time frequency identification system for a plethora of applications ranging from biomedical instrumentation, astronomy, radar jammers, etc.

## 5 Summary

We presented a comprehensive review of a host of basic ultrafast optical signal processing functionalities of

particular interest for IMWP applications utilizing compact, low latency WBGs. A detailed discussion on the design of silicon WBGs was also presented, including calculation of the physical design parameters for a specific target amplitude/phase response and the impact of fabrication imperfections on the ideal response. It is expected that we will see an increase in implementation of reconfigurable photonic integrated circuits for the generation and processing of high frequency and broadband RF signals, with frequencies/bandwidths into the THz range, by exploiting the unique advantages of monolithic SOI platform for applications in wireless communications, reconfigurable optical filtering of microwave signals, optical control of phased array antennas, microwave frequency measurement, among many others.

**Acknowledgements** We thank CMC Microsystems for enabling the fabrication of the silicon chips via ePIXfab, Lumerical Solutions Inc. for the design software and the NSERC SiEPIC CREATE Program. This research was supported in part by research grants from the FRQNT (Québec) and NSERC (Canada) agencies.

## References

1. Koenig S, Lopez-Diaz D, Antes J, Boes F, Henneberger R, Leuther A, Tessmann A, Schmogrow R, Hillerkuss D, Palmer R, Zwick T, Koos C, Freude W, Ambacher O, Leuthold J, Kallfass I. Wireless sub-THz communication system with high data rate. Nature Photonics, 2013, 7(12): 977–981
2. Eyre J, Bier J. The evolution of DSP processors. IEEE Signal Processing Magazine, 2000, 17(2): 43–51
3. Kuo S M, Lee B H, Tian W. Real-time Digital Signal Processing: Fundamentals, Implementations and Applications. New York: John Wiley & Sons, 2013
4. Seeds A J, Shams H, Fice M J, Renaud C C.Terahertz photonics for wireless communications. Journal of Lightwave Technology, 2015, 33 (3): 579–587
5. Nagatsuma T, Horiguchi S, Minamikata Y, Yoshimizu Y, Hisatake S, Kuwano S, Yoshimoto N, Terada J, Takahashi H. Terahertz wireless communications based on photonics technologies. Optics Express, 2013, 21(20): 23736–23747
6. Seeds A J. Microwave photonics. IEEE Transactions on Microwave Theory and Techniques, 2002, 50(3): 877–887
7. Iezekiel S. Microwave Photonics: Devices and Applications. New York: John Wiley & Sons, 2009
8. Capmany J, Novak D. Microwave photonics combines two worlds. Nature Photonics, 2007, 1(6): 319–330
9. Yao J. Microwave photonics. Journal of Lightwave Technology, 2009, 27(3): 314–335
10. Marpaung D, Roeloffzen C, Heideman R, Leinse A, Sales S, Capmany J. Integrated microwave photonics. Laser & Photonics Reviews, 2013, 7(4): 506–538
11. Roeloffzen C G, Zhuang L, Taddei C, Leinse A, Heideman R G, van Dijk P W, Oldenbeuving R M, Marpaung D A, Burla M, Boller K J. Silicon nitride microwave photonic circuits. Optics Express, 2013, 21(19): 22937–22961
12. Zhang W, Yao J. Silicon-based integrated microwave photonics. IEEE Journal of Quantum Electronics, 2016, 52: 1–12
13. Bogaerts W, De Heyn P, Van Vaerenbergh T, De Vos K, Kumar Selvaraja S, Claes T, Dumon P, Bienstman P, Van Thourhout D, Baets R. Silicon Microring Resonators. Laser & Photonics Reviews, 2012, 6(1): 47–73
14. Chrostowski L, Hochberg M. Silicon Photonics Design: From Devices to Systems. Cambridge: Cambridge University Press, 2015
15. Hill K O, Meltz G. Fiber Bragg grating technology fundamentals and overview. Journal of Lightwave Technology, 1997, 15(8): 1263–1276
16. Bazargani H P, Burla M, Chrostowski L, Azaña J. Photonic Hilbert transformers based on laterally apodized integrated waveguide Bragg gratings on a SOI wafer. Optics Letters, 2016, 41(21): 5039–5042
17. Burla M, Wang X, Li M, Chrostowski L, Azaña J. Wideband dynamic microwave frequency identification system using a low-power ultracompact silicon photonic chip. Nature Communications, 2016, 7: 13004
18. Burla M, Li M, Cortés L R, Wang X, Fernández-Ruiz M R, Chrostowski L, Azaña J. Terahertz-bandwidth photonic fractional Hilbert transformer based on a phase-shifted waveguide Bragg grating on silicon. Optics Letters, 2014, 39(21): 6241–6244
19. Burla M, Cortés L R, Li M, Wang X, Chrostowski L, Azaña J. On-chip programmable ultra-wideband microwave photonic phase shifter and true time delay unit. Optics Letters, 2014, 39(21): 6181–6184
20. Burla M, Cortés L R, Li M, Wang X, Chrostowski L, Azaña J. Integrated waveguide Bragg gratings for microwave photonics signal processing. Optics Express, 2013, 21(21): 25120–25147
21. Dolgaleva K, Malacarne A, Tannouri P, Fernandes L A, Grenier J R, Aitchison J S, Azaña J, Morandotti R, Herman P R, Marques P V. Integrated optical temporal Fourier transformer based on a chirped Bragg grating waveguide. Optics Letters, 2011, 36(22): 4416–4418
22. Rutkowska K A, Duchesne D, Strain M J, Morandotti R, Sorel M, Azaña J. Ultrafast all-optical temporal differentiators based on CMOS-compatible integrated-waveguide Bragg gratings. Optics Express, 2011, 19(20): 19514–19522
23. Bogaerts W, Selvaraja S K, Dumon P, Brouckaert J, De Vos K, Van Thourhout D, Baets R. Silicon-on-insulator spectral filters fabricated with CMOS technology. IEEE Journal of Selected Topics in Quantum Electronics, 2010, 16(1): 33–44
24. Othonos A. Fiber Bragg gratings. Review of Scientific Instruments, 1997, 68 (12): 4309–4341
25. Vivien L, Osmond J, Fédéli J M, Marris-Morini D, Crozat P, Damlencourt J F, Cassan E, Lecunff Y, Laval S. 42 GHz p.i.n germanium photodetector integrated in a silicon-on-insulator waveguide. Optics Express, 2009, 17(8): 6252–6257
26. Skaar J. Synthesis and Characterization of Fiber Bragg Gratings. Dissertation for the Doctoral Degree. Trondheim, Norway: Norwegian University of Science and Technology, 2000
27. Sima C, Gates J C, Holmes C, Mennea P L, Zervas M N, Smith P G. Terahertz bandwidth photonic Hilbert transformers based on synthesized planar Bragg grating fabrication. Optics Letters, 2013, 38(17): 3448–3451
28. Simard A D, Strain M J, Meriggi L, Sorel M, LaRochelle S.

Bandpass integrated Bragg gratings in silicon-on-insulator with well-controlled amplitude and phase responses. Optics Letters, 2015, 40(5): 736–739
29. Li M, Yao J. All-fiber temporal photonic fractional Hilbert transformer based on a directly designed fiber Bragg grating. Optics Letters, 2010, 35(2): 223–225
30. Simard A D, Belhadj N, Painchaud Y, LaRochelle S. Apodized silicon-on-insulator Bragg gratings. IEEE Photonics Technology Letters, 2012, 24(12): 1033–1035
31. Wiesmann D, David C, Germann R, Emi D, Bona G. Apodized surface-corrugated gratings with varying duty cycles. IEEE Photonics Technology Letters, 2000, 12(6): 639–641
32. Tan D T, Ikeda K, Fainman Y. Cladding-modulated Bragg gratings in silicon waveguides. Optics Letters, 2009, 34(9): 1357–1359
33. Hung Y J, Lin K H, Wu C J, Wang C Y, Chen Y J. Narrowband reflection from weakly coupled cladding-modulated Bragg gratings. IEEE Journal of Selected Topics in Quantum Electronics, 2016, 22 (6): 218–224
34. Wang X, Wang Y, Flueckiger J, Bojko R, Liu A, Reid A, Pond J, Jaeger N A, Chrostowski L. Precise control of the coupling coefficient through destructive interference in silicon waveguide Bragg gratings. Optics Letters, 2014, 39(19): 5519–5522
35. Cheng R, Chrostowski L. Multichannel photonic Hilbert transformers based on complex modulated integrated Bragg gratings. Optics Letters, 2018, 43(5): 1031–1034
36. Agrawal G P, Radic S. Phase-shifted fiber Bragg gratings and their application for wavelength demultiplexing. IEEE Photonics Technology Letters, 1994, 6(8): 995–997
37. Katsidis C C, Siapkas D I. General transfer-matrix method for optical multilayer systems with coherent, partially coherent, and incoherent interference. Applied Optics, 2002, 41(19): 3978–3987
38. Stoll H, Yariv A. Coupled-mode analysis of periodic dielectric waveguides. Optics Communications, 1973, 8(1): 5–8
39. Yariv A. Coupled-mode theory for guided-wave optics. IEEE Journal of Quantum Electronics, 1973, 9(9): 919–933
40. Streifer W, Scifres D, Burnham R. Coupling coefficients for distributed feedback single-and double-heterostructure diode lasers. IEEE Journal of Quantum Electronics, 1975, 11(11): 867–873
41. Zhang Y, Holzwarth N, Williams R. Electronic band structures of the scheelite materials $CaMoO_4$, $CaWO_4$, $PbMoO_4$, and $PbWO_4$. Physical Review B: Condensed Matter and Materials Physics, 1998, 57(20): 12738–12750
42. Lumerical FDTD, 2018
43. Pendry J. Photonic band structures. Journal of Modern Optics, 1994, 41(2): 209–229
44. Li Z Y, Lin L L. Photonic band structures solved by a plane-wave-based transfer-matrix method. Physical Review E: Statistical, Nonlinear, and Soft Matter Physics, 2003, 67(4 Pt 2): 046607
45. Applied Nanotools Inc., 2018
46. Simard A D, Beaudin G, Aimez V, Painchaud Y, Larochelle S. Characterization and reduction of spectral distortions in silicon-on-insulator integrated Bragg gratings. Optics Express, 2013, 21(20): 23145–23159
47. Ayotte N, Simard A D, LaRochelle S. Long integrated Bragg gratings for SOI wafer metrology. IEEE Photonics Technology Letters, 2015, 27(7): 755–758
48. Simard A D, Painchaud Y, LaRochelle S. Integrated Bragg gratings in spiral waveguides. Optics Express, 2013, 21(7): 8953–8963
49. Wang X, Yun H, Chrostowski L. Integrated Bragg gratings in spiral waveguides. In: Proceedings of Conference on Lasers and Electro-Optics (CLEO). San Jose, California: OSA, 2013, CTh4F.8
50. Ma M, Chen Z, Yun H, Wang Y, Wang X, Jaeger N A F, Chrostowski L. Apodized spiral Bragg grating waveguides in silicon-on-insulator. IEEE Photonics Technology Letters, 2018, 30 (1): 111–114
51. Simard A D, Ayotte N, Painchaud Y, Bedard S, LaRochelle S. Impact of sidewall roughness on integrated Bragg gratings. Journal of Lightwave Technology, 2011, 29(24): 3693–3704
52. Azaña J, Muriel M A. Real-time optical spectrum analysis based on the time-space duality in chirped fiber gratings. IEEE Journal of Quantum Electronics, 2000, 36(5): 517–526
53. Azaña J, Berger N K, Levit B, Fischer B. Spectral Fraunhofer regime: time-to-frequency conversion by the action of a single time lens on an optical pulse. Applied Optics, 2004, 43(2): 483–490
54. Yariv A, Yeh P. Photonics: Optical Electronics in Modern Communications. Oxford: Oxford University Press, 2006
55. Tong Y, Chan L, Tsang H. Fibre dispersion or pulse spectrum measurement using a sampling oscilloscope. Electronics Letters, 1997, 33(11): 983–985
56. Muriel M A, Azaña J, Carballar A. Real-time Fourier transformer based on fiber gratings. Optics Letters, 1999, 24(1): 1–3
57. Coppinger F, Bhushan A, Jalali B. Photonic time stretch and its application to analog-to-digital conversion. IEEE Transactions on Microwave Theory and Techniques, 1999, 47(7): 1309–1314
58. Chou J, Han Y, Jalali B. Adaptive RF-photonic arbitrary waveform generator. IEEE Photonics Technology Letters, 2003, 15(4): 581–583
59. Solli D, Chou J, Jalali B. Amplified wavelength–time transformation for real-time spectroscopy. Nature Photonics, 2008, 2(1): 48–51
60. Ouellette F. Dispersion cancellation using linearly chirped Bragg grating filters in optical waveguides. Optics Letters, 1987, 12(10): 847–849
61. Lepetit L, Chériaux G, Joffre M. Linear techniques of phase measurement by femtosecond spectral interferometry for applications in spectroscopy. Journal of the Optical Society of America B, 1995, 12(12): 2467–2474
62. Weiner A. Ultrafast Optics, volume 72. New York: John Wiley & Sons, 2011
63. Rivas L M, Strain M J, Duchesne D, Carballar A, Sorel M, Morandotti R, Azaña J. Picosecond linear optical pulse shapers based on integrated waveguide Bragg gratings. Optics Letters, 2008, 33(21): 2425–2427
64. Ashrafi R, Li M, Belhadj N, Dastmalchi M, LaRochelle S, Azaña J. Experimental demonstration of superluminal space-to-time mapping in long period gratings. Optics Letters, 2013, 38(9): 1419–1421
65. Li M, Dumais P, Ashrafi R, Bazargani H P, Quelene J B, Callender C, Azaña J. Ultrashort flat-top pulse generation using on-chip CMOS-compatible Mach–Zehnder interferometers. IEEE Photonics Technology Letters, 2012, 24(16): 1387–1389
66. Bazargani H P, Burla M, Azaña J. Experimental demonstration of sub-picosecond optical pulse shaping in silicon based on discrete space-to-time mapping. Optics Letters, 2015, 40(23): 5423–5426

67. Bazargani H P, Azaña J. Optical pulse shaping based on discrete space-to-time mapping in cascaded co-directional couplers. Optics Express, 2015, 23(18): 23450–23461
68. Bazargani H, Burla M, Chen Z, Zhang F, Chrostowski L, Azaña J. Long-duration optical pulse shaping and complex coding on SOI. IEEE Photonics Journal, 2016, 8(4): 1–7
69. Deng N, Liu Z, Wang X, Fu T, Xie W, Dong Y. Distribution of a phase-stabilized 100.02 GHz millimeter-wave signal over a 160 km optical fiber with $4.1 \times 10^{-17}$ instability. Optics Express, 2018, 26 (1): 339–346
70. Liu Y, Marpaung D, Choudhary A, Eggleton B J. Highly selective and reconfigurable $Si_3N_4$ RF photonic notch filter with negligible RF losses. In: Proceedings of Lasers and Electro-Optics (CLEO). San Jose, CA, USA: IEEE, 2017, paper SM1O.7
71. Fandiño J S, Muñoz P, Doménech D, Capmany J. A monolithic integrated photonic microwave filter. Nature Photonics, 2017, 11(2): 124–129
72. Zhuang L, Roeloffzen C G, Hoekman M, Boller K J, Lowery A J. Programmable photonic signal processor chip for radio frequency applications. Optica, 2015, 2(10): 854–859
73. Capmany J, Gasulla I, Pérez D. The programmable processor. Nature Photonics, 2016, 10: 6–8

**Saket Kaushal** received his bachelors in Electronics and Communication Engineering from IEM Kolkata, and M.S. (research) degree in Electrical Engineering from the Indian Institute of Technology Madras, India, in 2011 and 2016, respectively. He pursued his M.S. degree with the Integrated Optoelectronics Laboratory, under the supervision of Dr. Bijoy Krishna Das. After finishing his M.S., he worked in Applied Materials Inc. as a senior application engineer till July 2017. He is currently pursuing his Ph.D. degree with the Ultrafast Optical Processing group at the Institut National de la Recherche Scientifique–Centre Energie, Matériaux et Télécommunications, Université du Québec (Canada), under the supervision of Prof. José Azaña. His recent research interests include chip based energy efficient optical signal processors for high speed communication.

**Rui Cheng** received the B.Sc. degree from Shenyang Ligong University, Shenyang, China, in 2013, and the M.A.Sc. degree from Huazhong University of Science and Technology, Wuhan, China, in 2016. He is now working towards the Ph.D. degree in the Department of Electrical and Computer Engineering, the University of British Columbia (UBC), Vancouver, BC, Canada. His research interests lie in fiber optics and integrated optics. His current work focus on waveguide Bragg gratings.

**Minglei Ma** received his B.Sc. degree in Xidian University, China in 2010, and M. A.Sc. degree from Beijing University of Aeronautics and Astronautics, China in 2014. He is currently pursuing his Ph.D. degree in Electrical Engineering at University of British Columbia, Canada since 2014. His research interests include silicon photonic devices and systems, optoelectronics, for applications in optical communications.

**Ajay Mistry** received his B.A.Sc. degree in Electrical Engineering from the University of British Columbia (UBC), Vancouver, BC, Canada, in 2017. He is currently pursuing a Master's degree at UBC. His current work as a member of the photonics and optics research group at UBC, focuses on SOI-based wide-free-spectral-range filters and modulators for wavelength-division-multiplexing systems.

**Maurizio Burla** is a SNF Ambizione grantee at the Institute of Electromagnetic Fields (IEF) at ETH Zurich, Switzerland. He received his Ph.D. degree from the University of Twente, the Netherlands, where he worked on integrated optical beamformers for broadband phased array antenna systems. From 2012 to 2015, he has worked as a postdoctoral fellow at INRS-EMT, Montreal, Canada, on microwave and all-optical signal processing based on silicon photonic devices. His current research interests include integrated photonic and plasmonic technologies for microwave signal processing, mm-wave and sub-THz wireless communication systems, and electronic-photonic integration.

**Lukas Chrostowski** is a Professor of Department of Electrical and Computer Engineering at the University of British Columbia, Vancouver, BC, Canada. Born in Poland, he earned the B.Eng. degree in Electrical Engineering from McGill University and the Ph.D. degree in Electrical Engineering and Computer Science from the University of California at Berkeley. With research interests in silicon photonics, optoelectronics, high-speed laser (VCSEL) design, fabrication and test, for applications in optical communication systems, biophotonics and quantum information, he has published more than 200 journal and conference

publications. He co-edited a book "High-Speed Photonics Interconnects" (2013), and co-authored the book "Silicon Photonics Design" (Cambridge University Press, 2015). Dr. Chrostowski served as the co-director of the University of British Columbia AMPEL Nanofabrication Facility between 2008 and 2017. He was the Program Director the NSERC CREATE Silicon Electronic-Photonic Integrated Circuits (Si-EPIC) research training program in Canada (2012 – 2018), and has been teaching numerous silicon photonics workshops and courses since 2008. He spent his 2011 – 2012 sabbatical at the University of Washington, Seattle, with Michael Hochberg's group. Dr. Chrostowski received the Killam Teaching Prize at the University of British Columbia in 2014. He was an elected member of the IEEE Photonics 2014 – 2016 Society Board of Governors and served as the Associate VP of Education. He was awarded a Natural Sciences and Engineering Research Council of Canada Discovery Accelerator Supplements Award in 2015 for his research in silicon photonics integrated circuit design.

**José Azaña** received the Telecommunication Engineer degree (six years engineering program) and Ph.D. degree in Telecommunication Engineering from the Universidad Politécnica de Madrid (UPM), Spain, in 1997 and 2001, respectively. He has carried out scientific research work at the University of Toronto, the University of California at Davis, and McGill University in Montreal. Presently, he is a professor at the Institut National de la Recherche Scientifique – Centre Energie, Matériaux et Télécommunications (INRS-EMT) in Montreal/Varennes, where he holds the Canada Research Chair in "Ultrafast Photonic Signal Processing".

Prof. Azaña's research interests cover a wide range of topics, including ultrafast photonics, optical signal processing, fiber-optics and integrated-waveguide technologies, optical pulse shaping and waveform generation, optical telecommunications, all-optical computing, measurement of ultrafast events, light pulse interferometry, and broadband microwave signal generation, analysis and processing. He has to his credit more than 450 publications in top scientific journals and technical conferences, including above 200 contributions in high-impact peer-review journals (with most publications in the OSA, IEEE, and Nature Publishing Groups) and many invited and co-invited journal publications and presentations in leading international meetings. His published works have been highly cited by his peers.

Prof. Azaña is a Fellow Member of the OSA. He has served in the technical program committee of numerous scientific conferences and technical meetings, and he has been a Guest Editor for the EURASIP *J. Appl. Signal Proc.*, IEEE/OSA *J. of Lightwave Technol.*, *Chinese Science Bulletin*, and Elsevier *Opt. Comm.* Presently, he is an Associate Editor of *IET Electronics Letters*. Prof. Azaña's research outcome has been recognized with several research awards and distinctions, including the XXII national prize for the "best doctoral thesis in data networks" from the Association of Telecommunication Engineers of Spain (2002), the "extraordinary prize for the best doctoral thesis" from UPM (2003), the 2008 IEEE-Photonics Society (formerly LEOS) Young Investigator Award, and the 2009 IEEE-MTT Society Microwave Prize.